Seismic response of monopile foundations for offshore wind turbines: from 3D to 1D modelling of soil-foundation interaction

Dimitra Delavinia

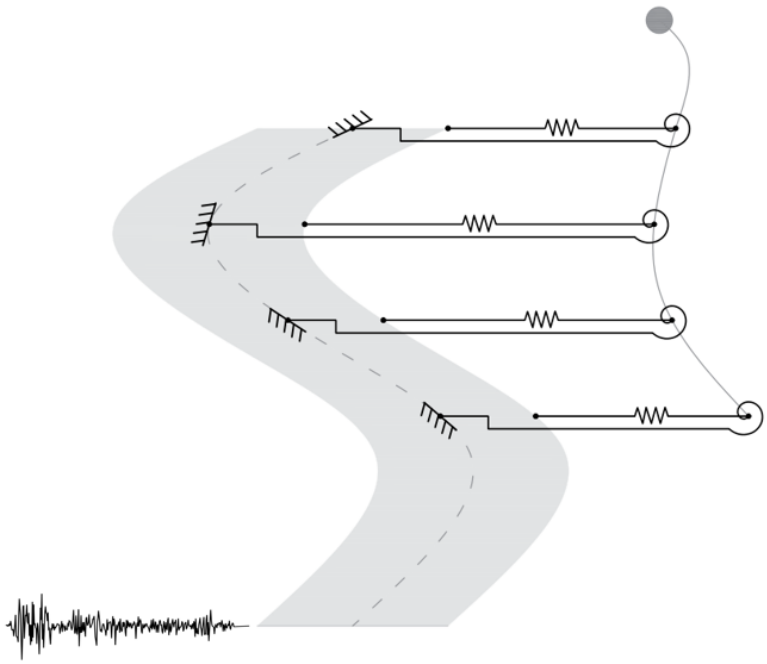

TU Delft Delft University of Technology

SIEMENS Gamesa RENEWABLE ENERGY

Seismic response of monopile foundations for offshore wind turbines: from 3D to 1D modelling of soil-foundation interaction

Master of Science Thesis

Author: Dimitra Delavinia (Student number: 5257441)

Supervisors:

Dr. ir. Federico Pisanò	TU Delft - Chair
Dr. ir. Apostolos Tsouvalas	TU Delft
Ir. Evangelos Kementzetzidis	TU Delft
Ir. Stavros Panagoulias	TU Delft, SGRE

September 22, 2022

TU Delft Delft University of Technology

SIEMENS Gamesa RENEWABLE ENERGY

Abstract

New offshore wind farms consisting of monopile-founded Offshore Wind Turbines (OWTs) are to be built in earthquake-prone areas. To design the monopile foundation and to accurately define the dynamic response of an OWT, the soil-monopile-superstructure interaction should be modelled properly. Due to the fact that the Three-Dimensional (3D) Finite Element (FE) analyses are complex and computationally expensive, research is focused on One-Dimensional (1D) FE models, in which the soil-monopile interaction is traditionally described via distributed translational springs representing the soil lateral load. Nevertheless, the increase of monopile diameter, followed by the monopile length-to-diameter ratio (L/D) decrease, implies the contribution of additional resistant components such as distributed moment, base shear and moment.

This thesis examines the 3D mechanisms to be accounted for in the 1D FE modelling of the soil-monopile-superstructure seismic response in case of a single-phased, linear visco-elastic soil layer. Both 3D and 1D FE analyses are conducted with the FE software OpenSees. The 1D analyses are simulated in two consecutive steps: first a Site Response Analysis is performed, next the recorded displacements over the soil layer depth are applied to the spring supports and the dynamic interaction of the system is simulated. Three different monopiles are considered with L/D equal to 26, 9 and 5. Two superstructures are examined, which are modelled as Single-Degree-of-Freedom systems. Distributed translational springs are assigned to the slender monopile (L/D=26), while for the stubbier monopiles the contribution of distributed rotational springs is examined as well. Lastly, the effect of considering the base moment and shear is also examined.

The stiffness of the soil reaction curves is calibrated by applying a monotonic lateral load and moment at the pile head, in case of the translational and rotational springs, respectively. The spring stiffness values are assumed uniform along the monopile

length. As a next step, the dynamic response of the calibrated 1D models is examined in steady-state conditions, under the action of mono-harmonic excitation, and compared to the 3D results. Ultimately, the seismic response of the 1D models is examined in case of two earthquake excitations with different frequency contents.

In case of the monopiles with L/D=9 and 5, it is concluded that the use of monotonically-calibrated distributed translational and rotational springs provides a good match between 3D and 1D regarding the monopile head and superstructure response under seismic loading. Nevertheless, these 1D FE models cannot predict the base moment, for which a base rotational spring should be employed. In case of the stubbier monopile, with L/D=5, the base shear seems to positively affect the moment profile as well. Lastly, regarding the monopile with L/D=26, the employment of translational springs alone seems sufficient for the accurate prediction of the seismic response; however, the hereby monotonically-calibrated distributed translational springs result in a mismatch between 3D and 1D.

Acknowledgements

First and foremost, I would like to thank my supervisors Federico Pisanò, Apostolos Tsouvalas, Vagelis Kementzetzidis and Stavros Panagoulias. Federico and Apostolos thank you for your insightful ideas and guidance. Vagelis and Stavros thank you for our weekly meetings, continuous support and advice. It has always been a pleasure to talk to you!

I would also like to thank Pim, Sachin and Joris for hosting the bi-weekly meetings in SGRE and of course all the SGRE students. It has been a pleasure to meet you all and share our small victories and difficulties throughout this process. Col, thank you for being pleasant all the time!

Last but not least, I would like to express my gratitude to my family and friends. Thank you all for being available and supportive when times got hard.

Dimitra Delavinia
Delft, September 2022

Contents

List of Figures

List of Tables

Nomenclature

Latin symbols

D	Monopile diameter, m
E_{p}	Monopile Young's modulus, kNm/m
E_{soil}, G_{soil}	Soil Young's modulus and shear modulus, kPa
$f_{\text{0,SSI}}$	First natural frequency of the soil-monopile-superstructure system, Hz
f_{FB}	Superstructure fixed-base frequency, Hz
I_{p}	Pile second moment of area, m^4
K_{r}	Dimensionless pile relative stiffness, $-$
$k_{\theta,av}$	Static m-θ spring stiffness calibrated based on monopile head moment loading and average-over-depth monopile rotation, kNm/m
k_{θ}	Static m-θ spring stiffness, kNm/m
$k_{y,av}$	Static p-y spring stiffness calibrated based on pile head lateral loading and average-over-depth deflection, kPa
$k_{y,head}$	Static p-y spring stiffness calibrated based on monopile head lateral loading and deflection, kPa
k_{y}	Static p-y spring stiffness, kPa
L	Monopile length, m
m	Distributed moment over monopile length, kNm/m
p	Distributed lateral load over monopile length, kN/m
U_{ff}	Lateral displacement at the free-field surface, m
u_{ff}	Amplitude of lateral displacement at the free-field surface (steady-state), m
U_{p}	Lateral displacement at the monopile head, m

u_p	Amplitude of lateral displacement at the monopile head (steady-state), m
U_{top}	Lateral displacement at the superstructure, m
u_{top}	Amplitude of lateral displacement at the superstructure (steady-state), m
V_{soil}	Shear wave propagation velocity, m/s
y	Lateral monopile displacement, m

Greek symbols

δ	Ratio $k_{\text{y}}/E_{\text{soil}}$, $-$
ω	Cyclic natural frequency, rad/s
θ_{p}	Amplitude of monopile head rotation (steady-state), rad

Abbreviations

1D	One-Dimensional
3D	Three-Dimensional
FE	Finite Element
OWT	Offshore Wind Turbine
SDOF	Single Degree of Freedom

Chapter 1

Introduction

1.1 Motivation for 1D seismic monopile design

Monopiles are single steel piles with large diameters, low length-to-diameter ratios and pipe cross-sections [23]. They are the most common foundation solution in the offshore wind industry, comprising 81% of the Offshore Wind Turbines (OWTs) foundations in 2019 [36]. This is attributed to their simple and cost-effective design, together with the vast knowledge regarding their installation [1, 27].

Nowadays, the offshore wind market is expanding to the Asia-Pacific region and the US; high-seismic areas [6]. The number of offshore wind farms which were already constructed and under development there, back in 2019, are presented in Figure 1.1, meaning that a great number of monopile-founded OWTs is expected to be subjected to seismic modelling.

Research shows that the seismic loading of monopiles may induce higher internal forces than the environmental loading [27], making their seismic design worth performing. While this can be accurately done by conducting Three-Dimensional (3D) Finite Element (FE) analyses, these are complex and computationally expensive. On the other hand, the One-Dimensional (1D) FE methods of the seismic soil-foundation interaction, which are based on the assumption of a Beam-on-Winkler-Foundation [8], are simpler and faster; therefore, constitute a valuable tool in the seismic design of monopile-founded OWTs.

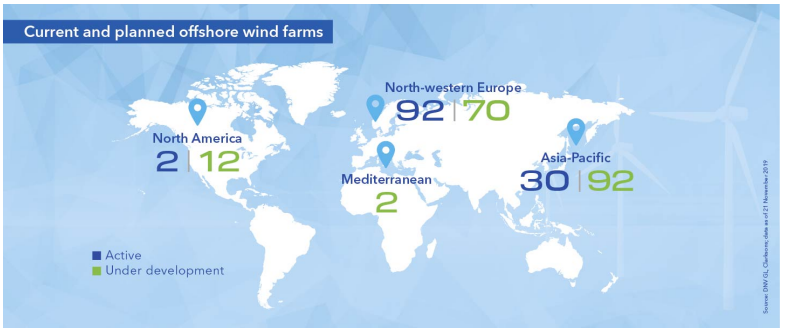

Figure 1.1: Current and planned offshore wind farms in 2019 [12]

1.2 1D seismic soil-pile-superstructure interaction

As already mentioned, the 1D modelling of soil-pile interaction is based on the assumption of a Beam-on-Winkler-Foundation, according to which the pile is modelled using 1D beam elements and the soil-pile interaction is represented by discrete translational springs connected to the beam nodes. The reactions on the nodes are local, meaning that they only depend on the lateral displacement (hereby denoted as y, in m) of the particular node [34]. They vary with y according to a soil-reaction curve, which is usually referred to as p-y, where p is the lateral distributed load (over the pile length), in kN/m.

To model a monotonically loaded beam, the other end of the springs (hereby called 'support') is fixed. However, for the dynamic soil-pile interaction, the soil layer deformation under the seismic excitation has to be accounted for. For this purpose, the 1D seismic modelling is done in two steps; hereafter called 'Step-1' and 'Step-2'. In Step-1, an 1D free-field site response analysis is performed, with the soil layer being excited by vertically propagating SH-waves [24]. In Step-2, the calculated total lateral displacements over depth are applied to the spring supports and the dynamic analysis is performed [8, 29]. Both steps are presented in Figure 1.2.

Assuming an idealized linear elastic soil, p-y curves have constant gradient, known as spring stiffness, in kPa. While in static loading a unique value of spring stiffness is employed, in case of dynamic loading the effect of the excitation frequency on the soil inertia is usually considered [2, 15]. Soils are not elastic materials; therefore, energy dissipation takes place. In case of soil-pile interaction, two sources of

damping are present; material and radiation damping, with the latter varying with frequency [15]. As a consequence, the actual system response is not in-phase with the applied dynamic load. To account for the phase lag between them, the spring stiffness of a linear elastic soil (known as 'impedance function') is expressed as a complex number which depends on the excitation frequency, damping and spring stiffness under static loading [15]. Section 1.2.1 presents methods for determining the static spring stiffness of a soil-pile system, hereby denoted as k_{y}.

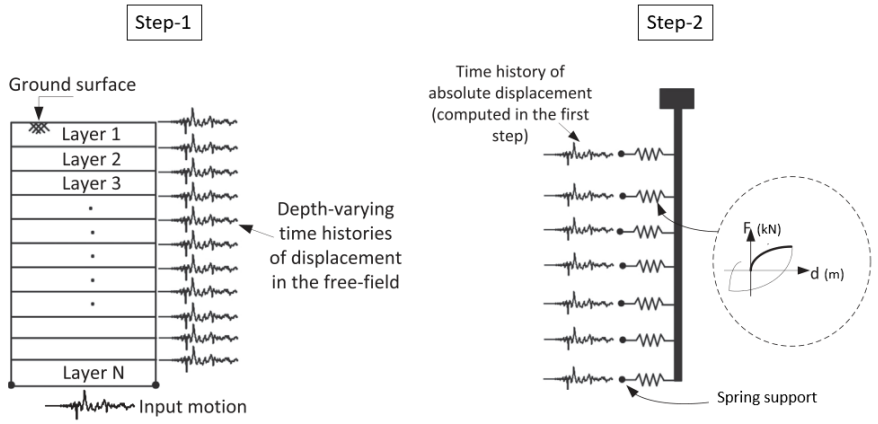

Figure 1.2: 1D modelling of seismic soil-pile-superstructure interaction (modified after Rahmani et al. [29])

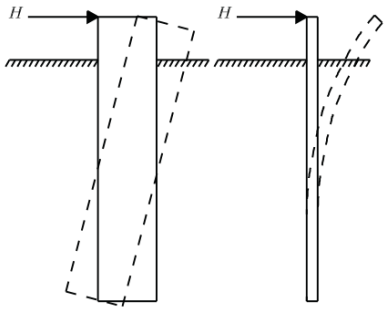

Figure 1.3: Rigid (left) and flexible (right) pile behaviour under lateral loading [31]

Although p-y springs are suitable for describing the bending of long flexible monopiles under lateral loading, this is not true for low length-to-diameter monopiles which

also rotate as rigid bodies under the action of a lateral load [10, 34], as illustrated in Figure 1.3. Details on the significance of additional reaction components regarding the lateral behaviour of non-slender monopiles are given in Section 1.2.2.

1.2.1 Static p-y spring stiffness values

The static spring stiffness, k_{y}, is usually determined as a proportion of the soil layer's Young's (E_{soil}) or shear modulus (G_{soil}). The ratio between k_{y} and E_{soil} is typically denoted as δ, uniform along the pile length. In the literature, different researchers suggest different values of k_{y}, depending on the soil-pile relative flexibility, pile geometry and response to be matched (e.g. pile head deflection, average deflection-over-depth).

Gazetas & Dobry [15] define δ, uniform over depth, as the one for which the pile head deflection under the action of a lateral head load is identical between 1D and 3D FE analyses. According to them, δ varies with the pile-to-soil stiffness ratio ($E_{\mathrm{p}}/E_{\mathrm{soil}}$), shape of pile cross-section (coefficient S), E_{soil} distribution over depth and pile head boundary condition (i.e. free-head, fixed-head). Their research is based on slender piles and constant k_{y} over depth is assumed. Focusing on the free-head piles, which is the case for the piles supporting OWTs, δ varies approximately between 1.5 and 2.5, as presented in Figure 1.4.

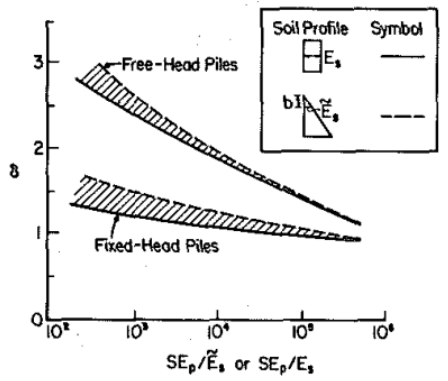

Figure 1.4: δ coefficient for slender piles matching the pile head deflection [15]

In another work it is proposed that the initial value of the subgrade modulus for a non-linear soil is approximated as $4G_{\mathrm{soil}}$ (or $\delta \sim$1.5) along the pile length [30]. This is based on the cavity expansion theory [25] -which applies to the problem of pile

installation- and on closed form solutions for static lateral pile head loading developed by Baguelin et al. [5]. The latter calculate k_{y} as the ratio between the sum of soil reactions and deflections along the pile length. Consequently, their solution results in values which are lower than the ones matching the pile head displacement [15].

Anoyatis et al. [2] study kinematically-stressed piles and conclude that a constant value of the real part of the impedance function is sufficient to model the variation of the pile head interaction factors with frequency. The δ values providing a good match between 3D and 1D in case of free-head and free-tip piles are reported in Table 1.1. It can be observed that δ corresponding to slender piles (e.g. $E_{\mathrm{p}}/E_{\mathrm{soil}}$ = 1000 and length-to-diameter = 20), is lower than the one matching the pile head deflection under pile head lateral loading [15] (Figure 1.4) and close to the 'average' δ values suggested by Randolph & Gourvenec [30], which is probably due to the type of loading applied in this work. Another note to make is that δ increases when $E_{\mathrm{p}}/E_{\mathrm{soil}}$ rises or the length-to-diameter ratio drops, implying that a higher value of lateral spring stiffness is expected for piles that behave more rigidly when being laterally loaded.

Table 1.1: δ values for free-head floating piles [2]

$E_{\mathrm{p}}/E_{\mathrm{soil}}$ [-]	Length-to-diameter ratio [-]	δ [-]
1000	5	2.5
	10	1.2
	20	1.2
10000	5	3
	10	2
	20	1.5

According to the PISA framework [9], the p-y curves are defined in case of monotonically loaded monopiles, with length-to-diameter ratios 2 to 6, founded in uniform sand. The initial stiffness of the curves is defined as linearly-dependent on the sand relative density and the depth-to-diameter ratio, with the stiffness decreasing from the mudline to the monopile base. In case of 75% relative density and a length-to-diameter ratio equal to 5, the initial spring stiffness is calculated as $8.64G_{\mathrm{soil}}$ and $4.59G_{\mathrm{soil}}$ at the monopile head and base, respectively.

According to the above-mentioned spring stiffness predictions, the pile diameter is not accounted for explicitly. In the literature, the findings regarding the p-y stiffness diameter-dependence are controversial for the slender piles, with some researchers

suggesting that k_{y} is diameter-independent [4] and others concluding that it increases linearly with the pile diameter [26]. The former consider the natural frequency prediction of the system, while the latter the pile head deflection under lateral pile head loading. Regarding the large-diameter non-slender monopiles, some researchers suggest that the diameter affects the initial p-y stiffness positively according to a power function, in case of horizontal quasi-static head loading for which the pile deflection-over-depth is matched [31].

1.2.2 Monopile soil reaction components

Whether a monopile will behave flexibly or rigidly under the action of a monotonic lateral load, depends on its rigidity relative to the soil. According to equation 1.1, the dimensionless pile relative stiffness (K_{r}) is calculated based on the soil and monopile Young's modulus, the monopile length and second moment of area (I_{p}). Rigid pile behaviour is expected if $K_{\mathrm{r}}>0.208$, while the behaviour is flexible if $K_{\mathrm{r}}<0.0025$ [1].

$$K_r = \frac{E_p I_p}{E_{soil} L^4} \tag{1.1}$$

As already described (Section 1.2.1), when laterally loaded, rigid monopiles deform in the horizontal direction but also rotate (Figure 1.3). Their rotation results in the development of vertical shear stresses from the surrounding soil and hence to distributed moments along their depth [10]. To account for this additional resisting mechanism, several researchers suggest the use of distributed moment-rotation springs, hereby denoted as m-θ [9, 10].

In addition to the m-θ springs, the contribution of both base shear force and moment is investigated in the literature [10, 20]. By matching 3D and 1D FE analyses, it is concluded that in case of non-slender monopiles under monotonic lateral head loading, the positive effect of base shear is similar to the one of base moment but lower than the one of distributed moment and lateral load [10]. In case of an isotropic poro-visco-elastic soil layer, it is found that the base shear effect becomes important for monopiles with a length-to-diameter ratio equal to 5, while for the base moment to affect the pile lateral resistance, ratios lower than 3 are needed [20].

All the aforementioned additional resistant components are also considered for caissons embedded in linear visco-elastic soil under lateral dynamic loading [17, 33], which are representative of very rigid (i.e. low length-to-diameter ratios) monopiles. A four-spring Winkler model is used, which apart from the distributed p-y springs,

employs distributed m-θ springs, together with a base translational and rotational spring.

1.3 Inertial and kinematic interaction effects

In case of linear elasticity, the seismic response of a soil-monopile-superstructure system can be expressed as the superposition of two effects, known as kinematic and inertial interaction effects [14, 32]. The kinematic interaction is defined as the soil-monopile interaction under the propagation of seismic waves, due to the stiffness difference between soil and monopile. In this case, both monopile and superstructure are considered massless. On the other hand, the inertial interaction is the interaction of the soil-monopile-superstructure system under the inertial loading of the system's mass imposed due to the kinematic interaction.

Figure 1.5 shows a typical pile head displacement and rotation response for kinematically loaded slender, free-head piles in steady-state conditions reached under the action of mono-harmonic vertically propagating waves as studied by Fan & Gazetas [13]. It is interesting to observe that a dimensionless frequency is used which accounts for the pile diameter and soil shear wave velocity, for which piles of different length-to-diameter ratios founded in the same soil layer practically have the same kinematic pile head deflection amplitude. The same is true for the pile head rotation, given the use of the dimensionless term $|\phi|d/u_{\text{ff}}$.

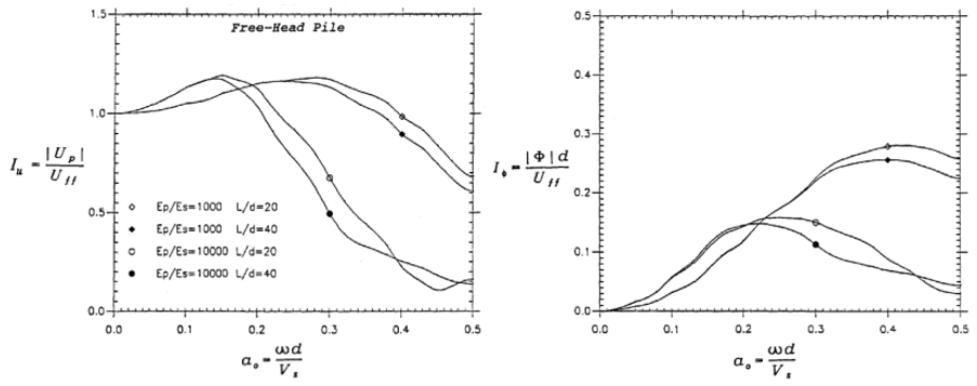

Figure 1.5: Soil-pile kinematic interaction with frequency (modified after Fan & Gazetas [13])

In Figure 1.6, a fixed-head pile with a Single-Degree-of-Freedom (SDOF) superstructure on top is examined considering the kinematic interaction, the inertial interaction and the dynamic interaction (i.e. combined kinematic and inertial) of the system, where H_{u} is the ratio of the pile head displacement amplitude over the free-field displacement amplitude. It is observed that the inertial interaction dictates the behaviour around the first natural frequency of the system (hereby denoted as $f_{0,\mathrm{SSI}}$), while kinematic interaction takes over for higher frequencies. The observed local amplification and de-amplification of the pile head response (i.e. H_{u} higher and lower than 1, respectively) around $f_{0,\mathrm{SSI}}$ is attributed to the change of phase lag between the superstructure and free-field lateral response [32]. This behaviour is further discussed later in the report.

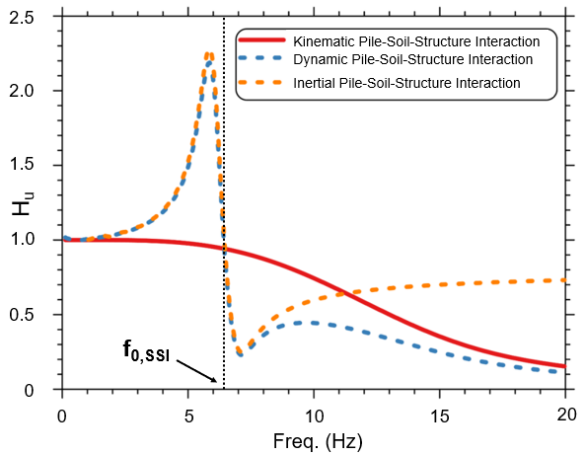

Figure 1.6: Soil-pile-superstructure interaction over frequency (modified after Turner et al. [32])

1.4 Thesis objective and problem definition

In this report, the seismic response of soil-monopile-superstructure systems is examined in both 3D and 1D FE models. Given that 1D FE models provide a simplified representation of the soil-monopile interaction, *the aim of this study is to identify the 3D mechanisms to be accounted for in 1D FE modelling, for different monopile geometries and superstructures in the linear elastic regime*.

This is done according to the following steps:

- First, the 3D dynamic soil-monopile-superstructure interaction with frequency is examined. Bottom mono-harmonic loading is applied and the response is evaluated in steady-state conditions;
- Second, the 1D reaction components are calibrated based on the 3D and 1D match for monotonic pile head loading;
- Third, the 3D and 1D match of the system dynamic interaction is assessed;
- Lastly, the 1D seismic response is compared to the one calculated with the 3D FE models and conclusions regarding the validity of the developed 1D FE models are reached.

In this context, three different thin-walled monopiles are considered, being free-tip and free-head. Their material and geometrical properties are shown in Table 1.2. Their total length equals their embedded length, meaning that the pile head is assumed to be at the soil layer surface. Based on K_{r} (Equation 1.1), the lateral behaviour of these piles is categorized as flexible and intermediate. This is illustrated in Figure 1.7. It is important to note that all the hereby examined piles fall into the margins of piles that have been used for the derivation of p-y curves or have been constructed in UK Offshore Wind Farms [1], meaning that they relate to the industry.

Table 1.2: Pile geometries examined

Notation	Diameter (D) [m]	Length (L) [m]	L/D [-]	Wall thickness [mm]	Pile Young's modulus (E_{p}) [GPa]	K_{r} (Eq.1.1) [-]	Pile-to-soil Young's modulus ($E_{\mathrm{p}}/E_{\mathrm{soil}}$) [-]
P1	0.67	17.5	26	19	210	2×10^{-5}	762
P2	2.0	17.5	9	20	210	5×10^{-4}	762
P3	7.5	36.0	5	75	210	5×10^{-3}	762

Two different superstructures are examined, as presented in Table 1.3. These are slender structures which behave as SDOF systems under the action of dynamic loading. Lastly, the soil layer is assumed to be single-phased, linear visco-elastic, having the geometric and material properties presented in Table 1.4. It lays on rigid rock and bottom excitation is applied at the rock surface.

The seismic interaction of the soil-monopile-superstructure systems is assessed for two earthquake excitations; the Kobe 1995 and Landers 1992, as recorded at the

Takatori and Lucerne Valley station, respectively. Their Fourier amplitude spectra are illustrated in Figure 1.8. As observed, these two excitations have different frequency contents, aiming at examining their effect on the 3D and 1D match of the system seismic response.

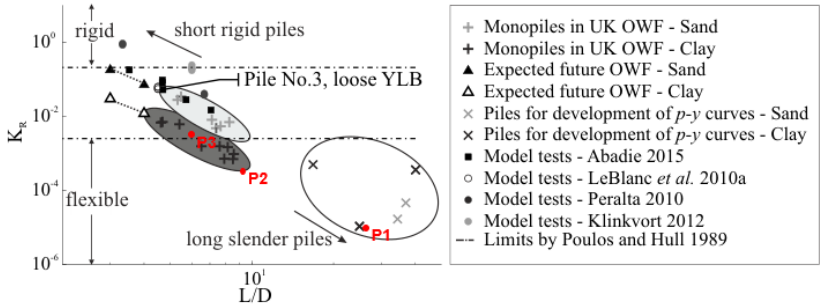

Figure 1.7: Pile relative stiffness (K_r) and length-to-diameter ratio values for realistic monopile design and piles used for the development of p-y curves (modified after Abadie [1])

Table 1.3: Superstructure geometries examined

Notation	Diameter [m]	Length [m]	Wall thickness [mm]	Mass [Mg]	Pile Young's modulus (E_p) [GPa]	Fixed-base frequency (f_{FB}) [Hz]
S1	0.67	8	19	50	210	1.13
S3	7.5	90	75	225	210	1.08

Table 1.4: Soil properties examined

Bulk density [Mg/m^3]	Shear wave velocity (V_{soil}) [m/s]	Poisson's ratio [-]	Young's modulus (E_{soil}) [MPa]	Layer thickness [m]	1st natural frequency [Hz]	Material damping [-]
1.84	240	0.30	276	50	1.20	0.05

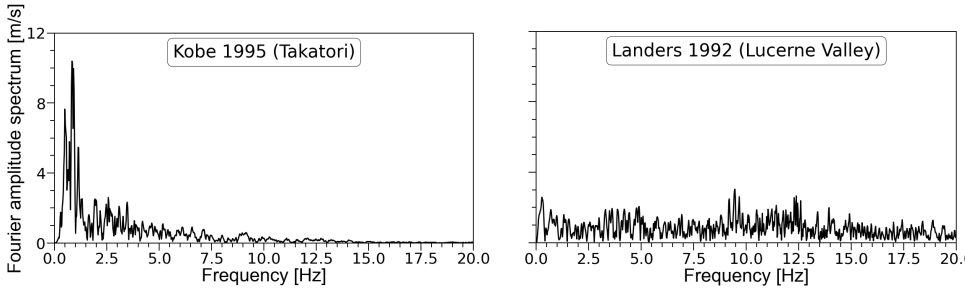

Figure 1.8: Fourier amplitude spectra for Kobe 1995 and Landers 1992 earthquake excitations

1.5 Outline

Based on the previously described objective, the outline of the thesis is structured as presented below:

Chapter 2 (3D Numerical modelling) describes the numerical methodology followed for the 3D FE analyses and presents the results of the steady-state dynamic soil-monopile-superstructure interaction for the different systems examined.

Chapter 3 (1D Numerical Modelling) describes the numerical methodology for the 1D FE analyses, examines the contribution and calibration of different soil reaction components in the prediction of the 3D system dynamic interaction and assesses the 1D FE model prediction of the system seismic response.

Chapter 4 (Conclusions & Recommendations) summarizes the findings of the report and suggests topics for future study.

Chapter 2

3D Numerical Modelling

2.1 Numerical methodology

The 3D modelling of the soil-monopile-superstructure interaction is performed with the FE software OpenSees (Open System for Earthquake Engineering Simulation). The soil continuum is modelled using one-phase 8-node standard brick ('8-node std-Brick') elements, with the linear elastic properties presented in Table 1.4. Both the monopile and superstructure are modelled using 1D linear Timoshenko beam elements (Tables 1.2 and 1.3, respectively). In case of the embedded beam elements, multiple horizontal rigid links connect the beam nodes to the surrounding soil nodes, simulating the area occupied by the pile. Pile and soil are considered fully bonded.

The shear beam boundary condition is applied at the lateral boundaries of the model (i.e. nodes of the same depth have the same lateral and vertical displacements, known as 'tied-node' boundary condition), while the vertical displacements at the bottom of the layer are fixed to simulate the underlying rigid rock. The lateral boundaries are placed at a distance of $25D$ from the pile axis, which is verified as sufficient for the simulation of the dynamic problem based on the wave propagation at the free-field and soil-monopile-superstructure interaction effects. The vertical size of the soil elements and time-step are defined based on Watanabe et al. [35]. In the horizontal direction, the mesh discretization is fine close to the pile, becoming coarser towards the lateral boundaries. A typical 3D FE mesh used in this study is illustrated in Figure 2.1.

Acceleration is applied at the bottom boundary and the analyses are performed in the time domain. Rayleigh damping is considered to simulate a practically constant material (viscous) damping (i.e. 5%, Table 1.4), throughout the frequency range of interest, by setting f_1 and f_2 equal to 1 and 10Hz, respectively.

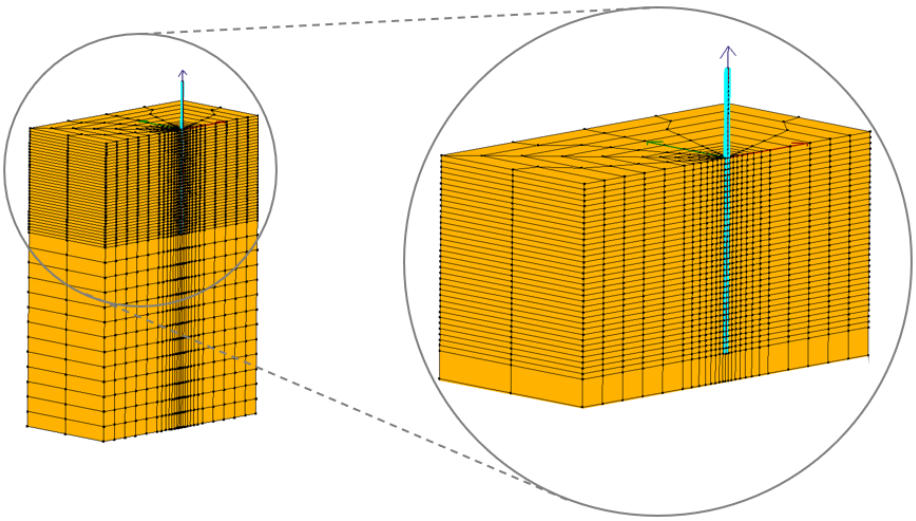

Figure 2.1: Typical 3D FE mesh in OpenSeesPL

2.2 Results

Piles P1, P2 and P3 are examined in combination with superstructure S1 (Tables 1.2 & 1.3). These pile-superstructure systems are hereafter called P1S1, P2S1 and P3S1, respectively. The soil-monopile-superstructure interaction is quantified by comparing the amplitude of the pile head and superstructure response to the free-field one in steady-state conditions using the following ratios, usually called 'interaction factors': $u_{\mathrm{p}}/u_{\mathrm{ff}}$, $\theta_{\mathrm{p}}/u_{\mathrm{ff}}$ and $u_{\mathrm{top}}/u_{\mathrm{ff}}$. The use of these factors eliminates the effect of the seismic excitation amplitude on the pile and superstructure response, given the assumption of linear elasticity. Figure 2.2 illustrates the definition of the parameters included in these factors.

In Figure 2.3, the dynamic interaction of these systems with frequency is illustrated.

Note that for the same soil-monopile-superstructure system, different excitation frequencies result in different system dynamic responses (i.e. different interaction factors). Furthermore, different systems exhibit different dynamic responses for the same excitation frequency. In all graphs, the first natural frequency of the system (denoted as $f_{0,\text{SSI}}$) is represented by a dotted line. The values of $f_{0,\text{SSI}}$ are given in Table 2.1. The stubbier the pile, the higher the $f_{0,\text{SSI}}$, which becomes practically equal to f_{FB} for the system P3S1.

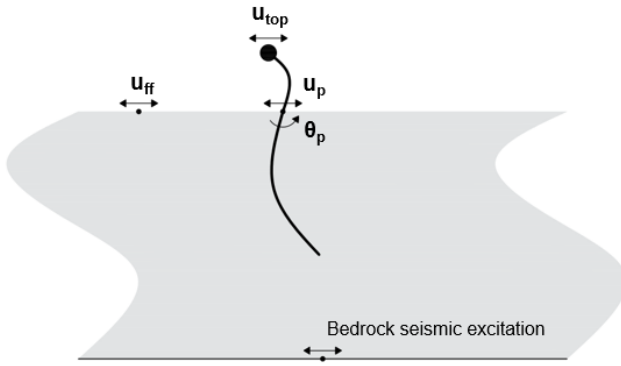

Figure 2.2: Superstructure, monopile and free-field amplitude response notation

Table 2.1: First natural frequency ($f_{0,\text{SSI}}$) of the soil-monopile-superstructure systems in 3D

System	$f_{0,\text{SSI}}$ [Hz]
P1S1	0.93
P2S1	1.10
P3S1	1.13

As expected, $u_{\text{top}}/u_{\text{ff}}$ is maximum at $f_{0,\text{SSI}}$ (i.e. resonance for an SDOF superstructure) for all piles. However, regarding $u_{\text{p}}/u_{\text{ff}}$, a local amplification and deamplification is observed around this frequency, a behaviour already described in Section 1.3. To understand this behaviour the phase lag between both u_{p} and u_{top} relative to u_{ff} is calculated for frequencies close to $f_{0,\text{SSI}}$. This is presented in Figure 2.4 where it is observed that, for all systems, the phase lag between u_{top} and u_{ff} is approximately 90 degrees at $f_{0,\text{SSI}}$. For lower frequencies, u_{top} and u_{ff} move in-phase (i.e. the phase lag is practically 0), while for higher frequencies, they move

out-of-phase with 180-degrees phase lag. These observations are in accordance with the dynamic behaviour of a fixed-base SDOF superstructure [11].

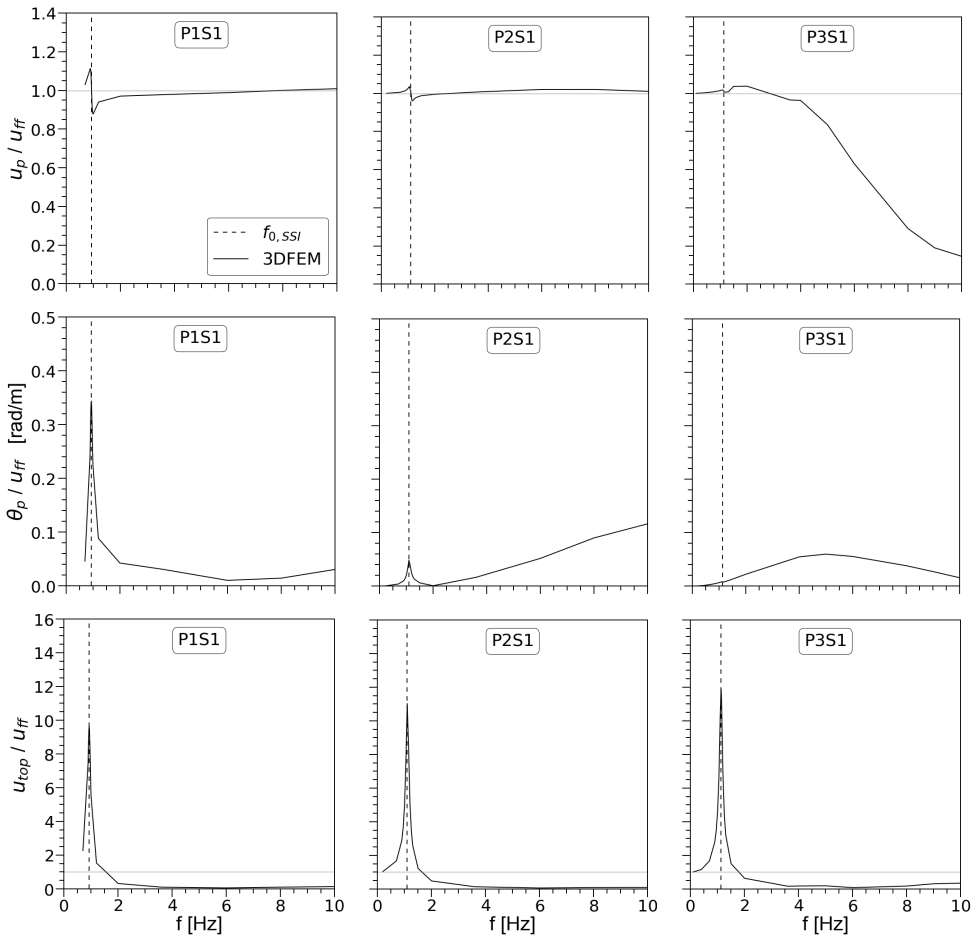

Figure 2.3: Variation of u_p/u_{ff}, θ_p/u_{ff} and u_{top}/u_{ff} with frequency for systems P1S1, P2S1 & P3S1

Regarding the u_p-u_{ff} phase angle, this is 0 degrees with the exception of frequencies in the vicinity of $f_{0,SSI}$ where the pile head is affected by the superstructure, concluding in a phase lag of around 30 degrees for P1S1 system. Of course, the stubbier

the pile, the lower the effect of the superstructure, hence for system P3S1 a uniform 0-degree phase angle is observed.

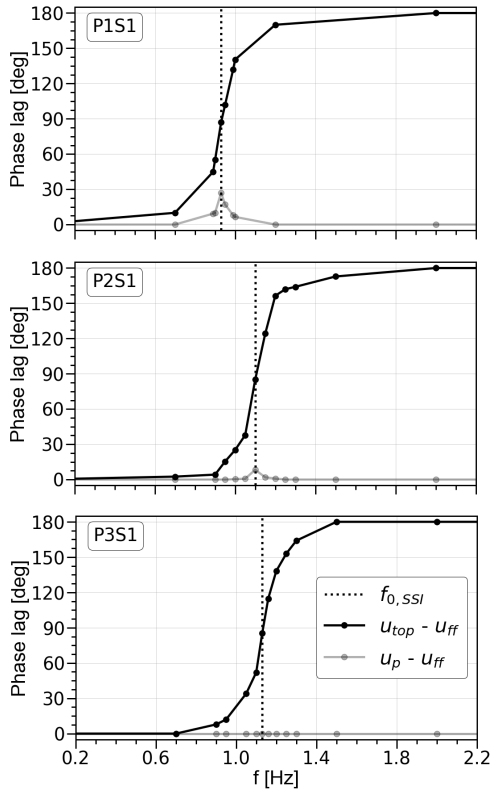

Figure 2.4: Phase angle of pile head and superstructure relative to the free-field

It can then be stated that the local maximum of the $u_{\mathrm{p}}/u_{\mathrm{ff}}$ graph occurs when superstructure and pile head are in-phase and u_{top} almost at its maximum value. Similarly $u_{\mathrm{p}}/u_{\mathrm{ff}}$ local minimum occurs when u_{top} is close to its maximum value and the superstructure starts moving out-of-phase relative to the pile head, meaning that the superstructure hinders the pile head displacement. It must be observed that the area where the pile is mostly affected by the superstructure (i.e. inertial interaction) is the widest for P1S1 and practically negligible for P3S1.

Regarding θ_{p}, all piles experience a local maximum at $f_{0,\mathrm{SSI}}$, which is attributed to

the system being at resonance with a base (i.e. pile head) being free to rotate. Note that the effect of the superstructure on pile P3 is so low that this local maximum is practically not present. Considering all the aforementioned observations, it can be stated that the inertial loading of the superstructure dictates the system response around $f_{0,\text{SSI}}$, as also stated by [32].

After the area around $f_{0,\text{SSI}}$ where the inertial effects are significant, the kinematic interaction of soil and monopile comes into play. This is due to the fact that with increasing excitation frequency, the free-field wave-length decreases. Hence, the pile is not able to follow the free-field movement and the interaction with the soil increases. Note that the inertial interaction is still present, however the kinematic interaction dominates the response. More details are given later in this section.

The pile not following the free-field displacement over depth results in u_p/u_ff factors that for certain frequencies are a bit higher than 1, but then drop to values lower than 1 (Figure 2.3). Significant kinematic interaction is represented by u_p/u_ff lower than 1. The stubbier the pile (i.e. higher K_r), the lower the frequency for which this occurs. In addition to this, P3 has greater length than P1 and P2. This is why, u_p/u_ff drops fast, almost immediately after $f_{0,\text{SSI}}$, for P3, while P1 follows the soil displacement along the examined frequency range (i.e. $u_\text{p}/u_\text{ff} = 1$).

The kinematic interaction also results in the rise of θ_p. Interesting is to note that θ_p and u_p do not increase accordingly. In other words, while u_p decreases, θ_p might be increasing. This has to do with the interaction between soil and pile. Figure 2.5 sheds light on the dynamic interaction over depth for systems P2S1 and P3S1. In this figure, the monopile-superstructure and free-field displacement are plotted over depth.

Considering pile P3, it can be seen that for an excitation frequency equal to 6.0Hz, the pile cannot follow the free-field displacement ($u_\text{p}/u_\text{ff} < 1$), however a small rotation is observed. For 10.0Hz, the pile gets almost vertical due to its high rigidity and the small wavelength relative to its length, resulting in the pile head rotation decline. Considering the same frequencies for pile P2, it can be seen that due to its smaller length and lower rigidity, $\theta_\text{p}/u_\text{ff}$ keeps increasing while the pile deflection over depth follows the deformation pattern of the free-field ($u_\text{p}/u_\text{ff} \sim 1$ for frequencies higher than $f_{0,\text{SSI}}$).

The importance of kinematic interaction for frequencies higher than $f_{0,\text{SSI}}$ is also verified in Figure 2.6 where u_p/u_ff and $\theta_\text{p}D/u_\text{ff}$ along the dimensionless frequency

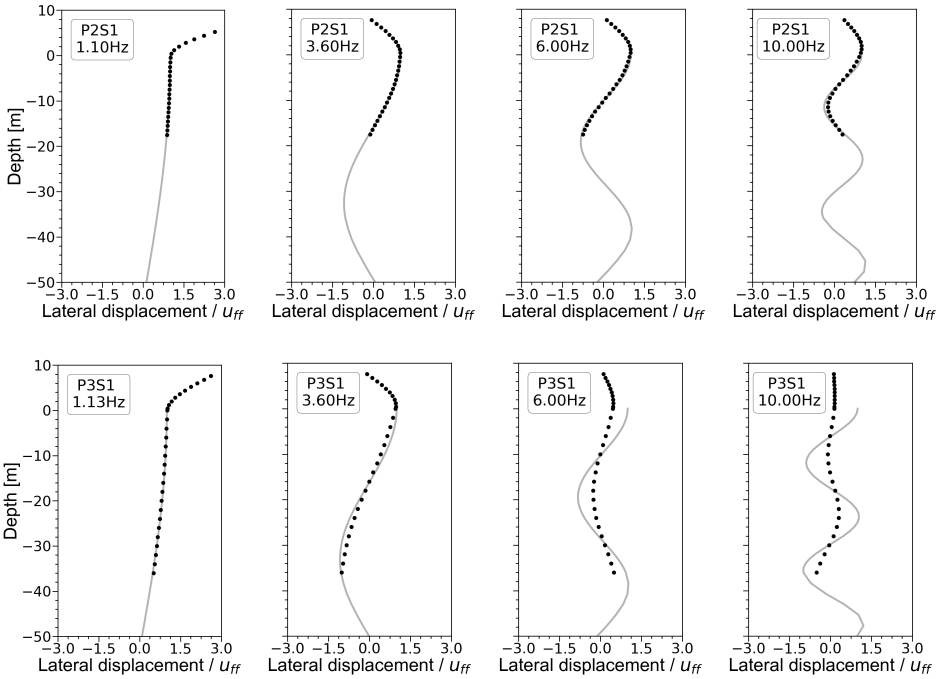

Figure 2.5: Free-field and monopile-superstructure lateral displacement over depth for different excitation frequencies, at maximum, u_{p}

$\omega D/V_{\mathrm{soil}}$ are plotted, with ω being the cyclic excitation frequency. This frequency normalization scheme accounts for the pile diameter and soil shear wave velocity and it is frequently used in the literature related to the kinematic interaction of piles [2, 13]. Note that the pile diameter is also accounted for in the pile head rotation interaction factor plotted in this graph. As observed, the curves of all of the three systems practically coincide for frequencies outside the area of significant inertial interaction, verifying that the inertial (i.e. mass) effects are negligible, and that the monopile and soil characteristics dictate the response.

Further insight on the kinematic and inertial interaction phenomena is given in Figures 2.7 and 2.8. Figure 2.7 shows the pile head response of P3 with different superstructures on top. In particular, apart form superstructure S1, superstructure S3 is examined as well (Table 1.3). Furthermore, pile P3 is considered ignoring its

mass and without any superstructure on top, aiming at modelling its kinematic interaction. First, it is observed that the P3S1 dynamic interaction is identical to the kinematic interaction of pile P3. This verifies that the inertial interaction is negligible for the system P3S1, as also observed in Figures 2.3 and 2.4, where no significant increase of $u_{\mathrm{p}}/u_{\mathrm{ff}}$ and $\theta_{\mathrm{p}}/u_{\mathrm{ff}}$ is observed around $f_{0,\mathrm{SSI}}$, while the pile head and free-field move in-phase.

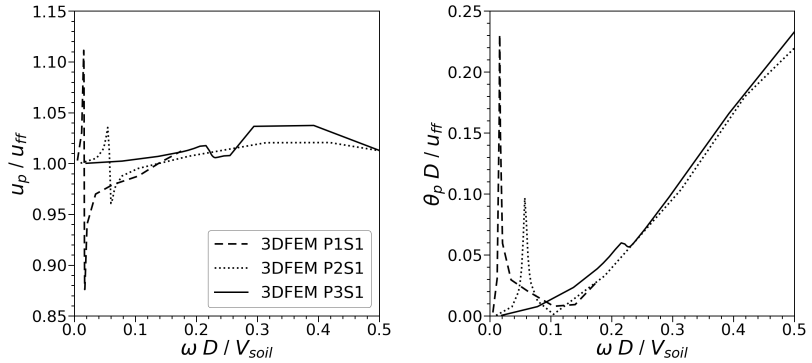

Figure 2.6: Variation of $u_{\mathrm{p}}/u_{\mathrm{ff}}$ and $\theta_{\mathrm{p}}D/u_{\mathrm{ff}}$ with $\omega D/V_{\mathrm{soil}}$

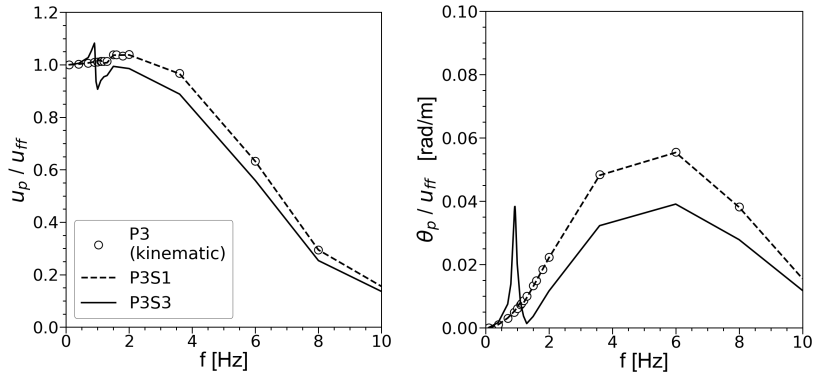

Figure 2.7: Inertial effects on pile head response

Superstructure S3 has a significantly higher mass and stiffness than S1 (Table 1.2). This results in higher inertial effects not only around $f_{0,\mathrm{SSI}}$ but also for higher frequencies. The inertial loading of the S3 mass results in $u_{\mathrm{p}}/u_{\mathrm{ff}}$ and $\theta_{\mathrm{p}}/u_{\mathrm{ff}}$ values

lower than for the kinematic interaction alone. This is attributed to the superstructure moving out-of-phase relative to the pile head (Figure 2.4) and hindering its response. Nevertheless, the kinematic interaction effect is more important after $f_{0,\mathrm{SSI}}$ as also stated by [32].

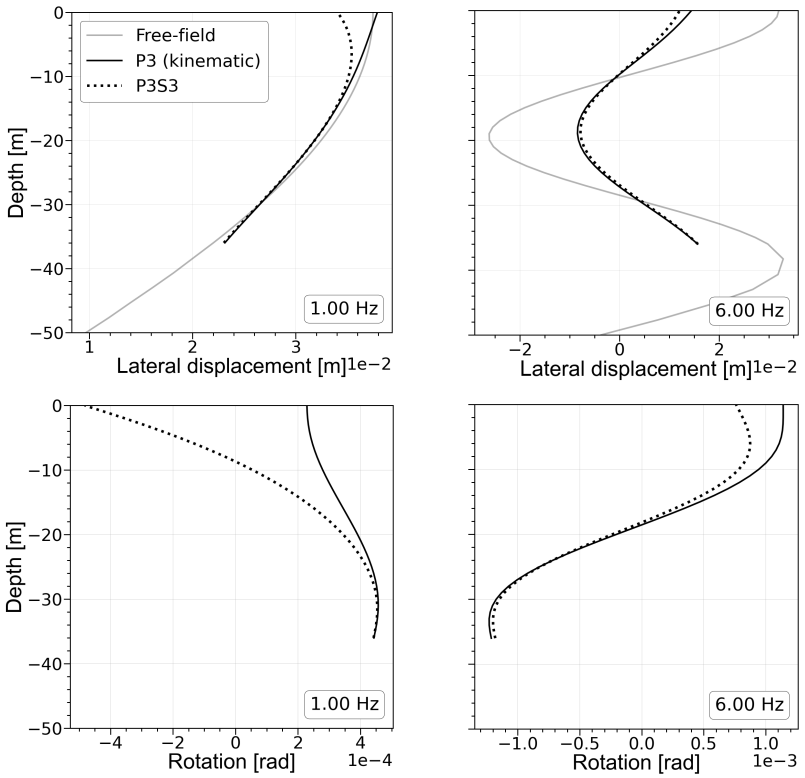

Figure 2.8: Inertial effects on monopile deflection and rotation profiles

The effect of inertial and kinematic effects along the pile depth are examined in Figure 2.8, where the pile deflection and rotation over depth (at maximum pile head displacement) for system P3S3 is illustrated with comparison to the kinematically-stressed pile P3. Frequencies 1.0 and 6.0Hz are examined, for which the inertial and kinematic effects dominate the dynamic response, respectively (Figure 2.7). Hence, this figure points out the effect of the superstructure mass loading on the pile deflec-

tion and rotation over depth, relative to the kinematic interaction effects.

As observed, the free-field deformation (i.e. kinematic loading) stresses the pile along its whole length. Adding a superstructure on top of the pile (system P3S3) alternates the deflection profile only at shallow depths, as already mentioned in the literature [14]. Of course, the effect is more prominent in case of 1.0Hz than for 6.0Hz, given that for these frequencies the inertial and kinematic interaction dominate the dynamic response, respectively. However, it is observed that the inertial loading of the superstructure affects the pile rotation to greater depths -not just near the pile head- especially for f=1.0Hz. These conclusions are expected to apply to monopile P2 as well.

Chapter 3

1D Numerical Modelling

3.1 Numerical methodology

In the 1D FE seismic modelling, the biggest uncertainty lies on the representation of the soil-monopile interaction; the soil reaction curves. As already mentioned, the hereby report explores the seismic interaction of soil-monopile-superstructure systems under the assumption of linear elasticity. Hence, the soil reaction curves are linear with a constant gradient; the spring stiffness.

The spring stiffness is calibrated based on the static soil-monopile interaction and used unchanged throughout the examined frequency range. This assumption is supported by [2], who conclude that δ calibrated under static conditions can be used in dynamic analyses as well. The calibration procedure of the soil reaction curves is hereafter referred to as Step-0.

In case of flexible pile behaviour, distributed p-y springs are employed alone and the static spring stiffness k_{y} is defined. This 1D FE model is hereafter referred to as *1-$spring$*. Nevertheless, to account for the rigid lateral behaviour of non-slender monopiles (Section 1.2.2), distributed rotational springs (with spring stiffness k_θ) are employed as well. These models are hereafter called *2-$spring$*. As an additional step, the effect of base shear and moment on the lateral resistance of non-slender piles is also examined.

After Step-0, two types of dynamics analyses are performed. First, the dynamic re-

sponse of the systems in steady-state conditions under the action of mono-harmonic bottom excitation (i.e. dynamic interaction) is simulated and compared to the one calculated with the 3D FE models (Chapter 2).

As a next step, the seismic response of the 1D FE models which make use of the already defined optimum calibrations is calculated in case of the Kobe and Landers earthquake excitations (Figure 1.8) and compared to the 3D FE response. The aim of this study is to assess the seismic response of the systems when real, multi-harmonic, earthquake excitations are considered. Further details on the configuration of the spring stiffness calibration and dynamic analyses are given in the upcoming sections.

3.1.1 Spring stiffness calibration

In this report, k_{y} and k_{θ} are calibrated based on monotonic loading with a pile head lateral force and pile head moment, respectively. Spring stiffnesses k_{y} and k_{θ} are considered uniform along the pile length -except for the springs both at the pile head and tip, where half the spring stiffness is assigned [18]- and their vertical distance is defined so as convergence of pile deflection and rotation under monotonic lateral loading is reached. In particular, a vertical size of 0.25m satisfies the convergence condition for both translational and rotational springs. Given the monotonic loading, the spring supports are fixed.

Two different values of k_{y} are defined so that either the pile head deflection or the average-over-depth pile deflection is matched between the 1D and 3D FE models. These are denoted as $k_{\mathrm{y,head}}$ and $k_{\mathrm{y,av}}$, respectively. In case of m-θ springs, the stiffness is calibrated based on the average-over-depth pile rotation alone (hereafter referred to as $k_{\theta,\mathrm{av}}$) considering at the same time the already calibrated p-y spring stiffness $k_{\mathrm{y,head}}$. A graphic representation of the p-y and m-θ stiffness calibration is shown in Figure 3.1.

The aim of the m-θ springs is to capture the rigid body rotation of the non-slender monopiles P2 and P3, under lateral loading. As observed in Chapter 2 (Figure 2.8), both inertial and kinematic interaction are expected to affect the monopile rotation over depth; hence the calibration considered herein accounts for the average-over-depth rotation instead of the pile head rotation. The suitability of considering $k_{\mathrm{y,head}}$ together with $k_{\theta,\mathrm{av}}$ instead of $k_{\mathrm{y,av}}$ - $k_{\theta,\mathrm{av}}$ or $k_{\mathrm{y,head}}$ - $k_{\theta,\mathrm{head}}$ is further examined in Appendix A.1, where the dynamic response of the system P2S1 in terms of pile head response with frequency is examined.

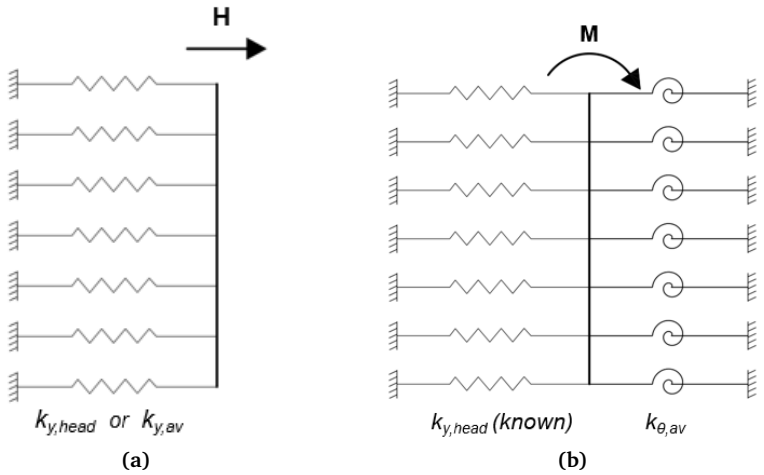

Figure 3.1: Spring stiffness calibration for (a) p-y and (b) m-θ springs

3.1.2 Dynamic analyses

According to the two-step procedure (Section 1.2), first the site response analysis of the soil column is performed (Step-1). The soil column is modelled using plane-strain quadrilateral elements and the 'tied-node' boundary condition is employed. Acceleration (i.e. either mono-harmonic or real earthquake excitation) is applied at the bottom boundary, which is fixed in the vertical direction, just as in the 3D model (Section 2.1). For each excitation frequency, the soil total displacements are recorded, to be later used in Step-2 (Figure 1.2). The vertical size of the elements is calculated as the minimum of: (a) the size calculated by [35] and (b) the beam element size for which convergence is reached under monotonic lateral loading (Section 3.1.1). Based on this vertical element size, the maximum time-step size to be used in dynamic analyses is calculated accoridng to [35].

In Step-2, the dynamic analysis of the soil-monopile-superstructure interaction is carried out. In this step, both monopiles and superstructures are modelled via 1D linear Timoshenko beam elements. The interaction between soil and foundation is described via distributed translational and/or rotational springs, already defined in Step-0. In case of the *1-spring* model, the recorded soil total displacements from Step-1 are applied at the spring supports and a dynamic analysis is performed for each excitation frequency (Figure 1.2). For the *2-spring* models, the rotations in-

duced by the free-field deflection over depth are also considered [17], as presented in Figure 3.2. This is done by calculating the tangent of the free-field deflection line.

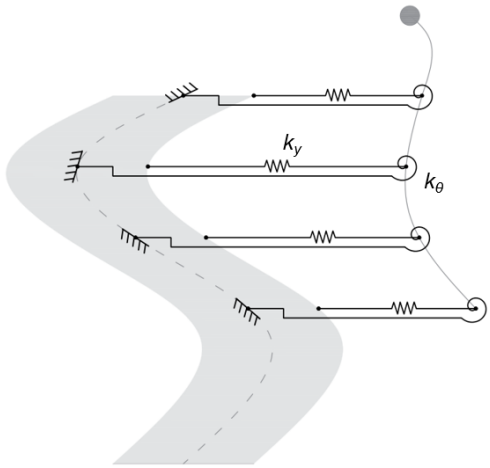

Figure 3.2: Modelling of 1D dynamic interaction when both translational and rotational springs are employed

The soil material (hysteretic) damping is accounted for by considering a 5% Rayleigh damping for f_1 and f_2 equal to 1 and 10Hz, respectively, same as for the 3D FE analyses (Section 2.1). Radiation damping is not modelled (i.e. no dashpots are considered). In the work of Anoyatis et al. [2], who examine the kinematic interaction of piles, it is concluded that the approximate representation of the radiation damping based on planar wave-propagation analysis [16] results in a mismatch between the 3D and 1D analyses, for frequencies higher than the cut-off frequency (i.e. first natural frequency) of the soil layer. On the contrary, considering the static spring stiffness coefficient alone results in a good match between the 3D and 1D prediction of the soil-monopile kinematic interaction no matter the excitation frequency.

The results of the 1D dynamic interaction and seismic response for the different spring models (i.e. $1\text{-}spring$, $2\text{-}spring$) and stiffness calibration procedures are presented in Section 3.2.2.

3.2 Results

3.2.1 Spring stiffness calibration

Table 3.1 contains the ratios $k_{\text{y}}/G_{\text{soil}}$ and $k_{\theta,\text{av}}/(G_{\text{soil}}D^2)$, as calculated according to the procedure described in Section 3.1.1. Given that monopile P1 is categorized as a slender pile (Figure 1.7), it will mainly bend under the action of lateral loads. Hence, the additional distributed moment resistant mechanism (Section 1.2.2) which applies to the non-slender monopiles is not valid in this case and only translational p-y springs are considered.

Monopiles P2 and P3 have the same $k_{\theta,\text{av}}/(G_{\text{soil}}D^2)$ value, proving that the moment resistant mechanism depends on D^2. This confirms the relation to the outside area of the pile and the shear stresses developing there, leading to the development of distributed moment (Section 1.2.2). Another conclusion is that, for the two monopiles examined herein with different D and L/D values, the latter does not affect k_θ (Tables 3.1 and A.1). In the literature, the stiffness of the distributed moment-rotation springs is found dependent on the L/D ratio of caisson foundations [17, 33]. With that in mind, monopiles of lower L/D ratios should be examined to assess whether the L/D ratio affects k_θ for monopiles stubbier than the ones examined herein.

Table 3.1: Calculated spring stiffness values

Pile	$k_{\text{y,head}}/G_{\text{soil}}$ [-]	$k_{\text{y,av}}/G_{\text{soil}}$ [-]	$k_{\theta,\text{av}}/(G_{\text{soil}}D^2)$ [-] (for $k_{\text{y,head}}$)
P1	6.5	2.8	-
P2	7.0	3.0	1.3
P3	7.5	3.8	1.3

According to Table 3.1, $k_{\text{y,head}}$ is always higher than $k_{\text{y,av}}$, as expected (Section 1.2.1). Furthermore, the calculated k_{y} values are in general similar to the ones suggested in the literature. In particular, $k_{\text{y,head}}$ for the slender monopile P1 is in agreement with [15], while all $k_{\text{y,av}}$ values are close to the ones suggested by [2, 30]. Lastly, regarding monopile P3, the spring stiffness value calculated based on the pile head deflection falls within the values predicted by PISA [9] over depth (Section 1.2.1); however it is lower than their prediction for the pile head spring stiffness. This has probably to do with the fact that in the hereby report the stiffness is assumed uniform over depth, while in [9] k_{y} is considered depth-dependent.

Figure 3.3 illustrates how k_{y} varies with diameter. It is observed that no matter the

calibration method, the p-y spring stiffness increases with D. Regarding $k_{\text{y,av}}$, it increases practically linearly with D, while for $k_{\text{y,head}}$ a non-linear relationship seems to be the case. Note that for the monopiles examined herein, the diameter increase comes with an L/D decrease. The hereby k_{y} values cannot be compared to the literature findings on the diameter effect where slender and non-slender monopiles are examined separately (Section 1.2.1). A greater number of monopiles of various diameters and rigidities should be examined to conclude on the diameter and L/D effect. Nevertheless, the rise of k_{y} for stubbier piles is in agreement with the observations of [2].

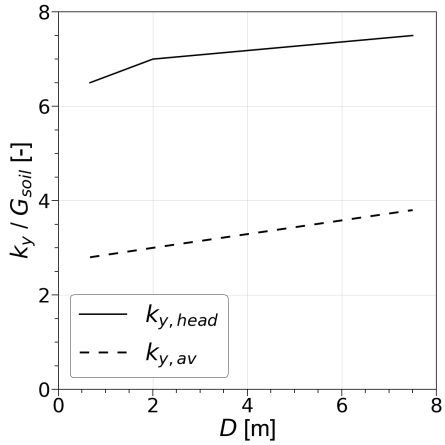

Figure 3.3: p-y spring stiffness variation with pile diameter

3.2.2 Dynamic analyses

3.2.2.1 Systems dynamic interaction

In this section, the dynamic interaction of the systems examined in Chapter 2 is simulated using the already calibrated 1D spring models (Section 3.2.1).

Figure 3.4 illustrates the dynamic response of systems P1S1, P2S1 and P3S1 in case of the traditional *1-spring* models in steady-state conditions with the use of the interaction factors already defined in Section 2.2. Two different spring stiffnesses are examined; $k_{\text{y,head}}$ and $k_{\text{y,av}}$, which are calculated in Section 3.2.1.

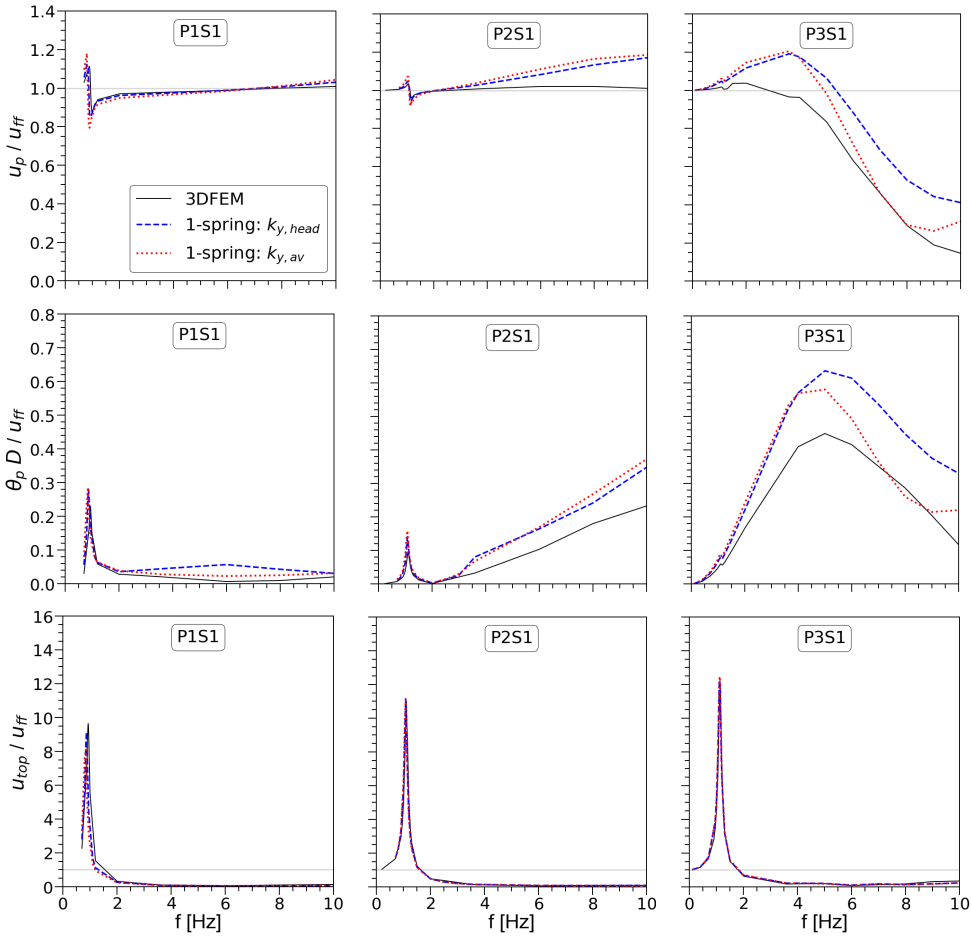

Figure 3.4: P1S1, P2S1 & P3S1 dynamic interaction for the *1-spring* models

It is observed that in case of system P1S1, a good match between 3D and 1D is in general achieved with either of the two *1-spring* models. This is attributed to the fact that P1 is flexible, hence it mainly deflects under the seismic loading and p-y springs are sufficient to simulate the soil-monopile interaction. Focusing at the pile head and superstructure lateral displacement amplitude around $f_{0,\text{SSI}}$, it is observed that $k_{\text{y,head}}$ results in better predictions of the 3D values given the dominance of in-

ertial loading; however it overestimates θ_p for frequencies higher than $f_{0,SSI}$. The latter is better approximated by $k_{y,av}$ and this is attributed to the monopile's being significantly kinematically-loaded over depth (Section 2.2).

In case of the stubbier monopile P2, the effectiveness of *1-spring* models clearly worsens with frequency. Around $f_{0,SSI}$, the spring stiffness $k_{y,head}$ results in a good match between 3D and 1D for the pile head deflection and rotation and superstructure displacement amplitude, as expected, given the dominance of inertial loading (Section 3.1.1). Outside the area where the superstructure mass affects mostly the pile head behaviour, u_p and θ_p are significantly overestimated. In contrast to P1S1, $k_{y,av}$ does not provide a good match for these frequencies, verifying that the lateral resistance of monopile P2 comprises lateral load p but distributed moment m as well (Section 1.2.2), especially for frequencies where the kinematic interaction dominates the response.

The same conclusions are in general reached for the system P3S1. However, for excitation frequencies higher than around 6.0Hz, $k_{y,av}$ does provide a better match between 3D and 1D for u_p and θ_p. This behaviour is explained by referring to Figure 2.5, according to which monopile P3 remains practically vertical, meaning that the distributed moment resistant mechanism becomes less important. Comparing now the dynamic response of system P3S1 with the one of P3S3 which is presented in Figure 3.5, it can be observed that the effectiveness of *1-spring* models seems to be slightly affected by the superstructure mass on top of the monopile, given the out-of-phase movement relative to the pile head which hinders θ_p (Figure 2.7), making the *1-spring* models relatively more effective in case of P3S3.

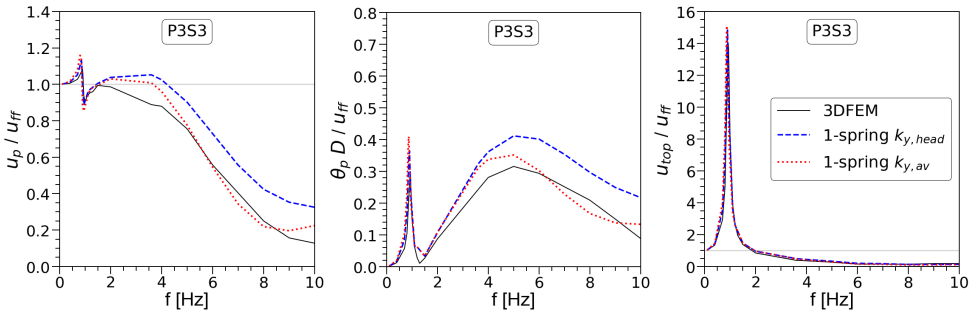

Figure 3.5: P3S3 dynamic interaction for the *1-spring* models

As *1-spring* models prove in general insufficient for modelling the dynamic inter-

action of non-slender piles (i.e. systems P2S1, P3S1 and P3S3), the contribution of the distributed moment resistant mechanism is examined, employing distributed m-θ springs in addition to the p-y springs. These are the *2-spring* models, already described in Section 3.1.1. For these models, $k_{\text{y,head}}$ is used, as it provides a better prediction of $u_{\text{p}}/u_{\text{ff}}$ and $\theta_{\text{p}}/u_{\text{ff}}$ around $f_{0,\text{SSI}}$ (Figure 3.4), given the inertial loading of the upper part of the monopile and the subtle kinematic interaction effects (Section 2.1). On the other hand, m-θ springs are calibrated based on the average rotation-over-depth under monotonic loading, aiming at capturing the rigid rotation of non-slender monopiles throughout the examined frequency range and especially where kinematic interaction dictates the dynamic response. The values of the spring stiffnesses are presented in Table 3.1.

The 1D FE results for systems P2S1, P3S1 and P3S3 when *2-spring* models are used, are illustrated in Figure 3.6 with a blue dashed line. It can be seen that by employing m-θ springs a better agreement between 3D and 1D is achieved. Although the *2-spring* model gives 1D results almost identical to 3D in case of system P2S1, when it comes to systems P3S1 and P3S3 the pile head rotation is slightly under-predicted for frequencies higher than $f_{0,\text{SSI}}$. This means that the consideration of the same rotational spring stiffness overestimates the contribution of the moment-rotation resistant mechanism at these frequencies in case of monopile P3, implying that the m-θ stiffness for the dynamic interaction might be L/D-dependent.

In the same figure (Figure 3.6), the results for a lower m-θ spring stiffness are presented with a red dotted line. This spring stiffness is hereby denoted as $k_{\theta,\text{dyn}}$ and is calibrated so that the *2-spring* model provides a sufficiently good match between 3D and 1D for both u_{p} and θ_{p} throughout the examined frequency range. A stiffness of $1.0G_{\text{soil}}D^2$ seems to work for both monopiles P2 and P3. In addition to these analyses, the dynamic response of the system P2S1 in case of different combinations of spring stiffnesses k_{y} and k_{θ} are examined in Appendix A.1, proving the suitability of the hereby suggested calibration procedure based on monotonic pile head loading (Section 3.1.1).

From both Figures 3.6 and A.1 it is concluded that the rotational spring stiffness affects the match between 3D and 1D mostly at frequencies higher than $f_{0,\text{SSI}}$, in accordance with the observations made earlier regarding the small value of monopile rotation around $f_{0,\text{SSI}}$ (Figure 2.8). This implies that the distributed moment resistant mechanism is more important for frequencies where the kinematic interaction dominates the response.
Based on the results already presented in Figures 3.4 to 3.6, it can be declared that,

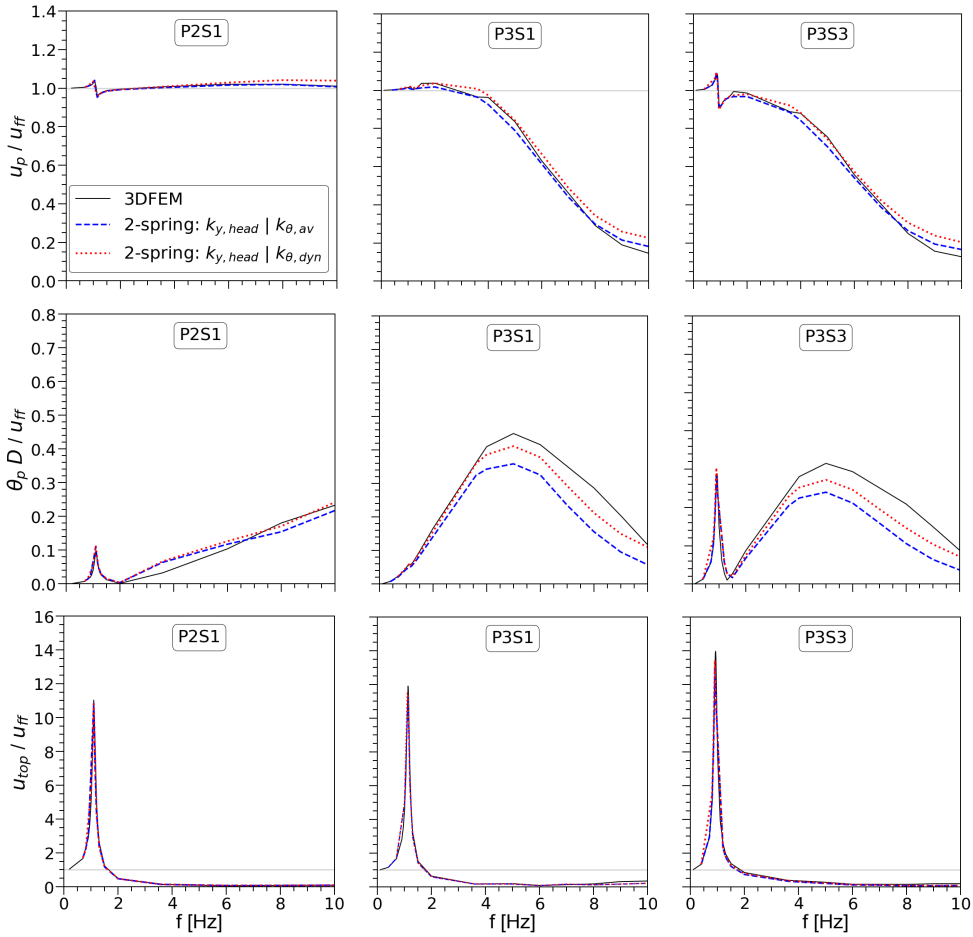

Figure 3.6: P2S1, P3S1 & P3S3 dynamic interaction for the *2-spring* models

in general, the *1-spring* and *2-spring* models represent quite accurately the 3D pile head and superstructure response in case of the slender monopile P1 and the non-slender piles P2 and P3, respectively. Additionally, their effectiveness in predicting the monopiles' response over depth is examined in the following figures.

Figure 3.7 shows the deflection and moment distribution for monopile P1 for the

excitation frequency 1.20Hz (i.e. 1st natural frequency of the soil layer) where u_p is maximum. According to this figure, a successful prediction of the response over depth is achieved with either of the two *1-spring* models. Of course, the observations regarding the advantage of $k_{y,head}$ around $f_{0,SSI}$ (Figure 3.4) apply to this figure as well. The moment and deflection profiles are also examined in case of an excitation frequency higher than $f_{0,SSI}$, 6.0Hz, for which the kinematic interaction dominates the response and the monopile is stressed over depth. These results are presented in Appendix A.2.1 where it can be seen that the developed base moment is not captured.

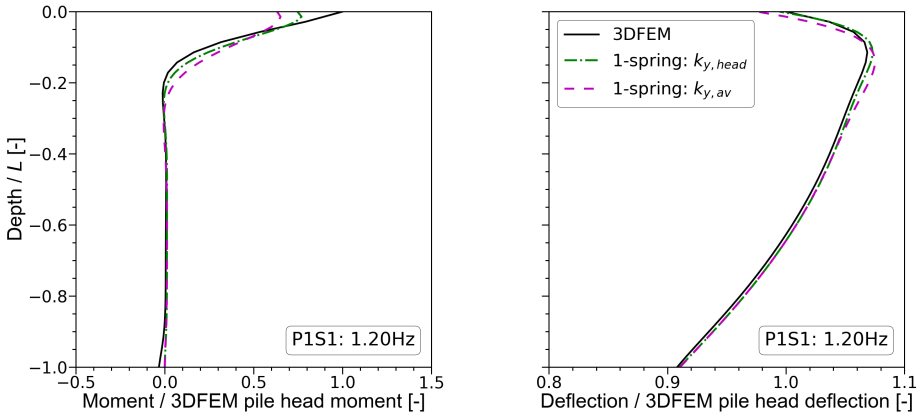

Figure 3.7: P1S1 moment and deflection profiles at maximum pile head displacement (f = 1.20Hz)

In Figure 3.8 the deflection and moment distribution over the monopile length for the system P2S1 in case of maximum pile head displacement is shown. It can be seen that using the *2-spring* models in general enhance the predictions of the 1D FE models regarding the monopile response over depth. Nevertheless, the inherent deficiency of the hereby employed 1D FE models to predict the real pile base moment has to be noted. Similar conclusions are reached in case of a 6.0Hz mono-harmonic excitation, as presented in Appendix A.2.1.

In case of P3S1 and P3S3, the *2-spring* models give, in general, better predictions of the moment and deflection values near the pile head in comparison to the ones by *1-spring* models, as illustrated in Figure 3.9 for f=1.20Hz and in Figures A.4, A.5

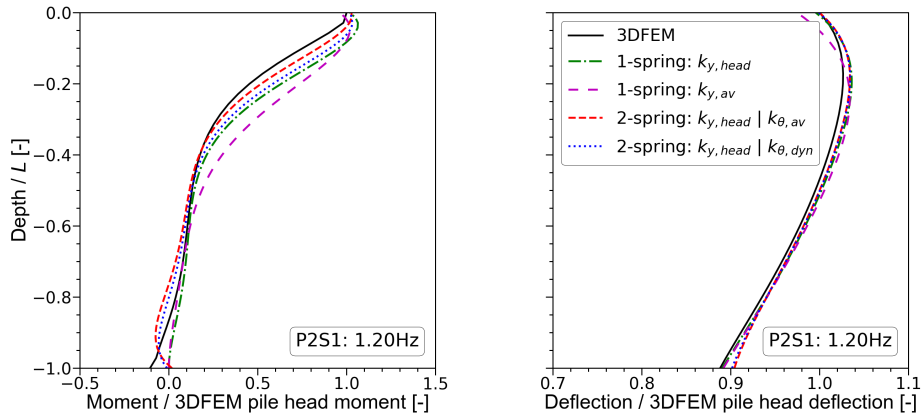

Figure 3.8: P2S1 moment and deflection profiles at maximum pile head displacement (f = 1.20Hz)

for f=6.0Hz. However, the already mentioned inherent deficiency of the *1-spring* and *2-spring* models to predict the base moment and shear leads to a divergence between the 3D and 1D predictions at the pile tip, which, as expected, affects the pile moment and deflection distribution to higher depths.

Given the abovementioned observations, the effect of a base translational spring is examined in case of systems P3S1 and P2S1, hereby denoted as $K_{\text{y,base}}$ and calculated as a proportion of G_{soil} and D. Next, a base moment-rotation spring is employed as well, denoted as $K_{\theta,\text{base}}$ and calculated as a proportion of G_{soil} and D^3. It is assumed that given the consideration of the diameter in the calibration of these stiffnesses, the same spring stiffness equations apply to both monopiles P2 and P3. Similar relations are considered for the base resistance of caisson foundations [33]. Nevertheless, it has to be noted that the aim of the hereby analyses is to examine the base effect relative to the *2-spring* models, not to calibrate the base translational and rotational springs.

Figures 3.10 and 3.11 illustrate the contribution of the base translational and rotational springs to the moment and deflection profiles for systems P2S1 and P3S1 at maximum pile head displacement (i.e. f=1.20Hz). According to these results the base effect seems less important for the monopile P2 than the monopile P3, as the change of the moment and deflection profiles is small. This is in agreement with

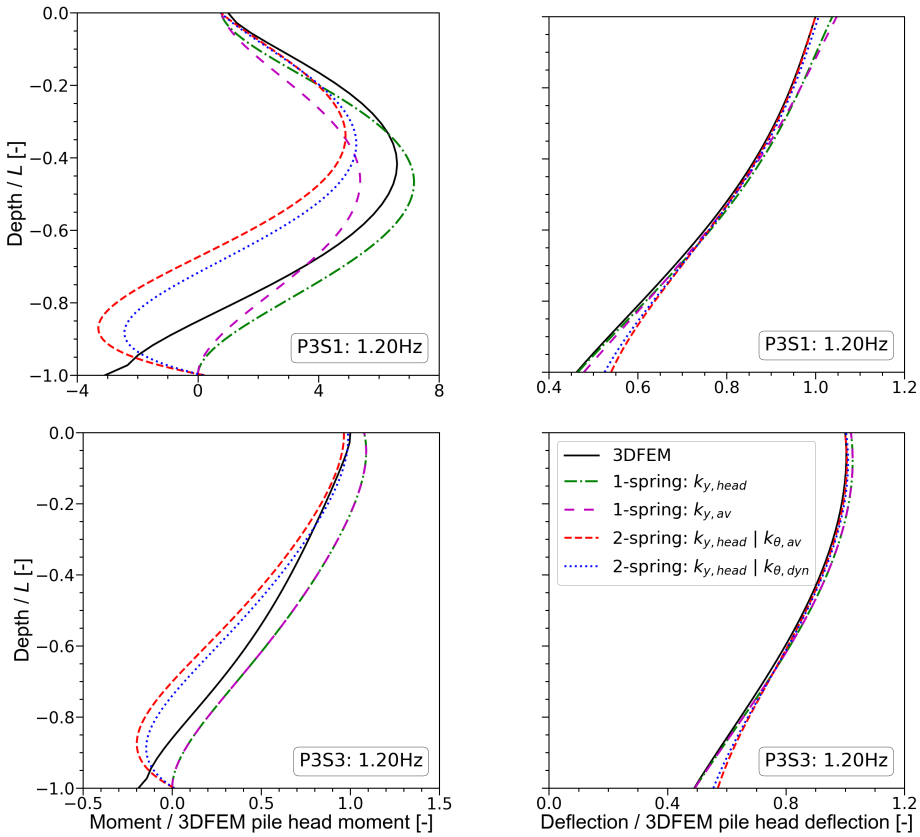

Figure 3.9: P3S1 & P3S3 moment and deflection profiles at maximum pile head displacement (f = 1.20Hz)

the results of [20]. Similar conclusions are reached in case of 6.0Hz mono-harmonic excitation (Appendix A.2.2).

Regarding the contribution of the base moment (brown line) relative to the base shear (cyan line) in the prediction of the moment and deflection profiles of monopile P3 in case of 1.20Hz and 6.0Hz (Figures 3.11 and A.7), it can be concluded that the base shear is more significant than the base moment, when considering the overall moment and deflection distribution. However, to capture the base moment, a base

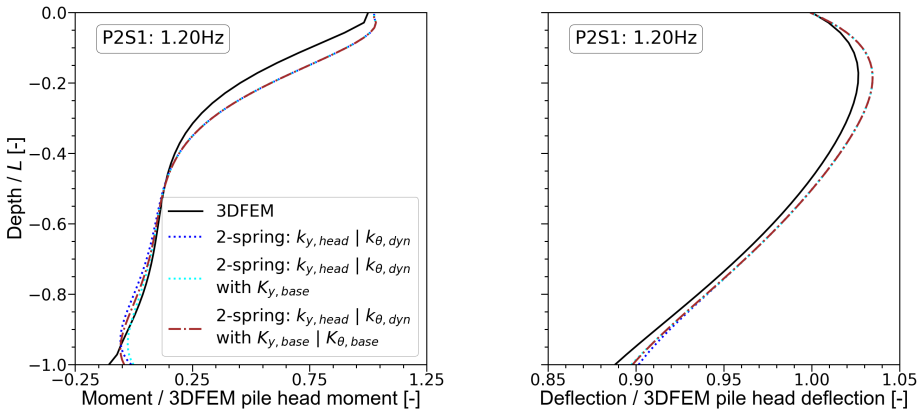

Figure 3.10: Base effect at maximum pile head displacement (f = 1.20Hz) for P2S1

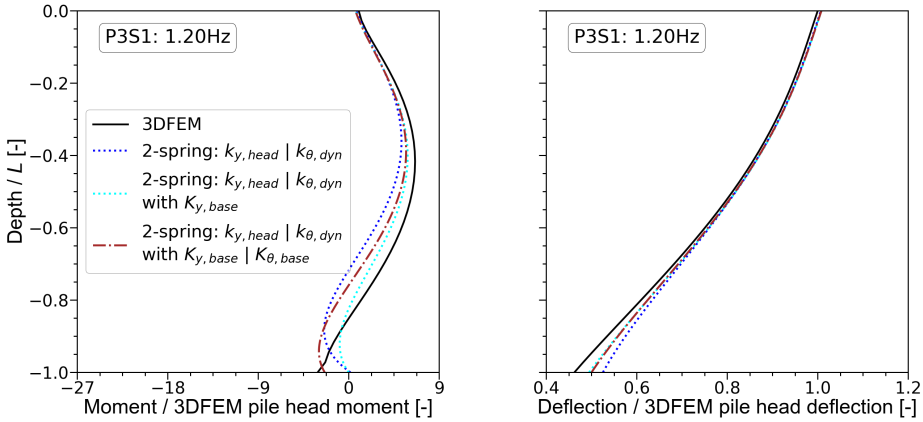

Figure 3.11: Base effect at maximum pile head displacement (f = 1.20Hz) for P3S1

rotational spring should be employed.

3.2.2.2 Systems seismic response

In Section 3.2.2.1 it is concluded that the *1-spring* and *2-spring* models calibrated based on monotonic pile head loading provide a good prediction of the pile head and superstructure amplitude response in case of the slender monopile P1 and the

non-slender monopiles P2 and P3, respectively. However, for the moment and deflection profiles to be accurately simulated, the base resistant components seem to have an important effect in case of P3.

In this section, the previously calibrated *1-spring* and *2-spring* models are employed and the seismic response is examined in case of the earthquakes Kobe and Landers (Figure 1.8). The same Rayleigh damping is applied for both excitations; the one used earlier with a damping ratio equal to 5% at f_1=1.0Hz and f_2=10.0Hz. These earthquake excitations have different frequency contents aiming at shedding light on their effect on the predictions by the previously calibrated 1D models. It has to be noted that, given the assumption of linear elasticity, the difference in the amplitude of these excitations does not affect the conclusions regarding the match between 3D and 1D.

Figures 3.12 to 3.15 show the pile head lateral displacement (U_{p}), rotation (Θ_{p}) and superstructure displacement (U_{top}) with time for systems P1S1, P2S1, P3S1 and P3S3. Starting from the non-slender monopiles P2 and P3, it is observed that the 1D models provide a good prediction of the pile head and superstructure response, proving that the suggested calibration for the *2-spring* models results in good match between 3D and 1D for both steady-state (i.e. dynamic interaction, Section 3.2.2.1) and seismic response.

The moment and deflection profiles at maximum pile head displacement of systems P2S1 and P3S1 are presented in Figures 3.17 to 3.19. It is observed that the match between 3D and 1D in case of the deflection profiles is good. Nevertheless, in case of the moment distribution, the base moment is not captured; therefore affecting the moment distribution to lower depths, especially for P3S1. The employment of a base rotational spring is expected to enhance the prediction of the 1D models; however, this is not examined herein. Comparing Figures 3.18 and 3.19, it can be concluded that the superstructure affects the prediction of the moment profile by the 1D FE models. This is not the case for the already examined dynamic interaction where the systems are in steady-state (Figure 3.9).

Moving to the slender monopile P1 and system P1S1, it can be seen that the match between the 3D and 1D analyses is considered insufficient (Figure 3.12). This mismatch is probably due to the incapability of the hereby assigned *1-spring* models to predict the real 1$^{\text{st}}$ natural frequency of the P1S1 system. In particular, while $f_{0,\text{SSI}}$ equals 0.93Hz, the 1D FE models prediction is 0.87 and 0.83Hz in case of $k_{\text{y,head}}$ and $k_{\text{y,av}}$, respectively. In addition to this, as already seen in Section 3.2.2.1, the *1-*

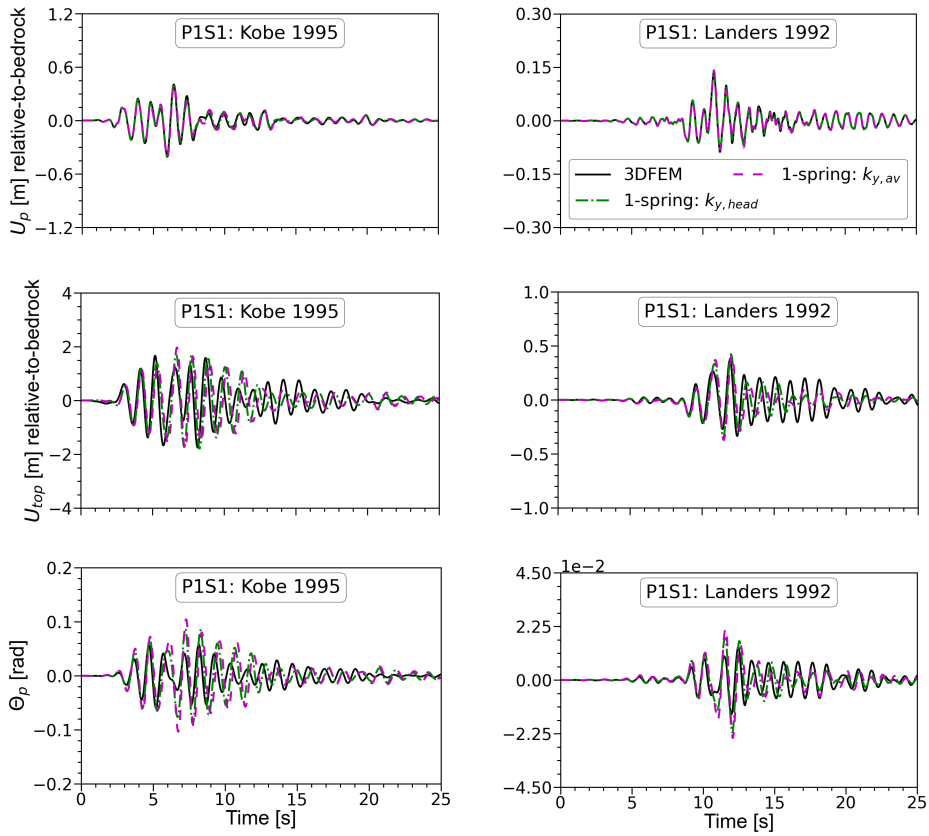

Figure 3.12: P1S1 pile head and superstructure time histories for earthquakes Kobe and Landers

spring models do not provide a perfect match for the pile head rotation. These two drawbacks are probably the reason behind the 3D-1D mismatch when the seismic response is modelled.

Lastly, regarding the moment and deflection profiles at maximum pile head displacement for monopile P1 (Figure 3.16), it can be observed that, as seen before, the match between 3D and 1D is generally good, with the exception of the pile head moment.

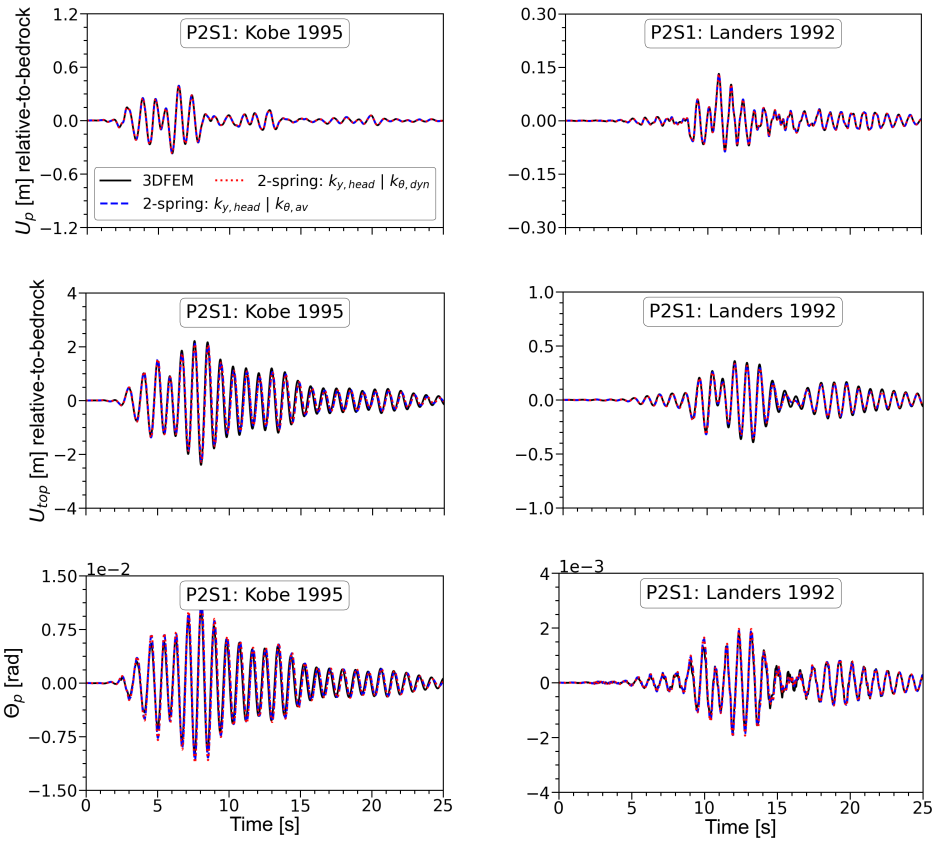

Figure 3.13: P2S1 pile head and superstructure time histories for earthquakes Kobe and Landers

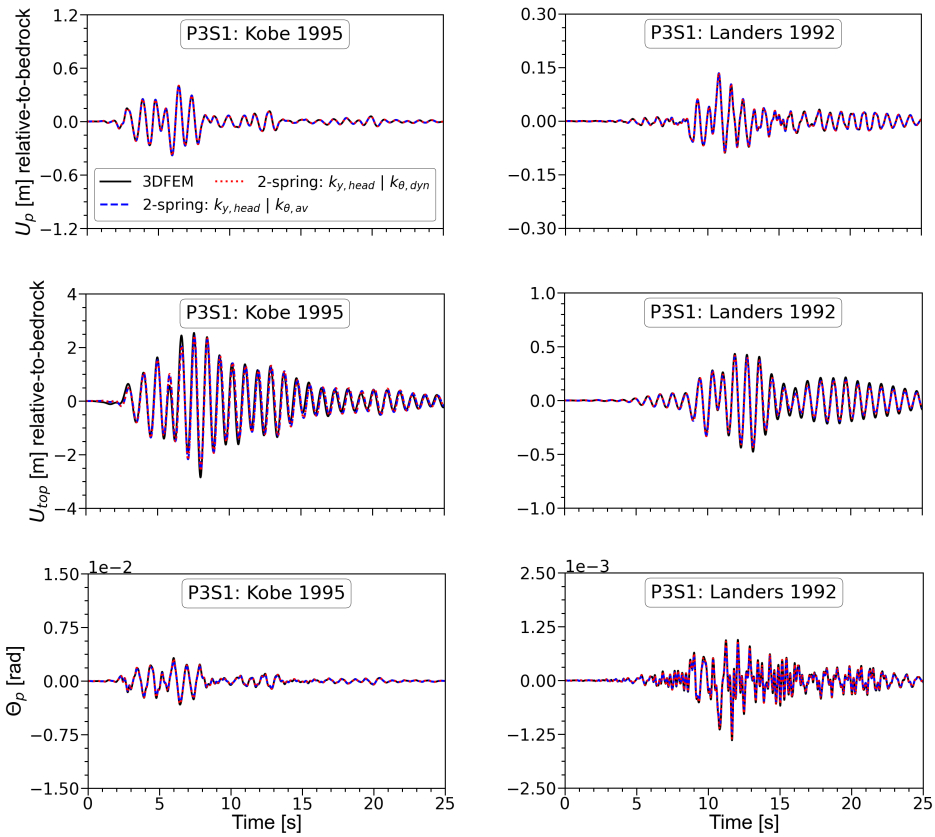

Figure 3.14: P3S1 pile head and superstructure time histories for earthquakes Kobe and Landers

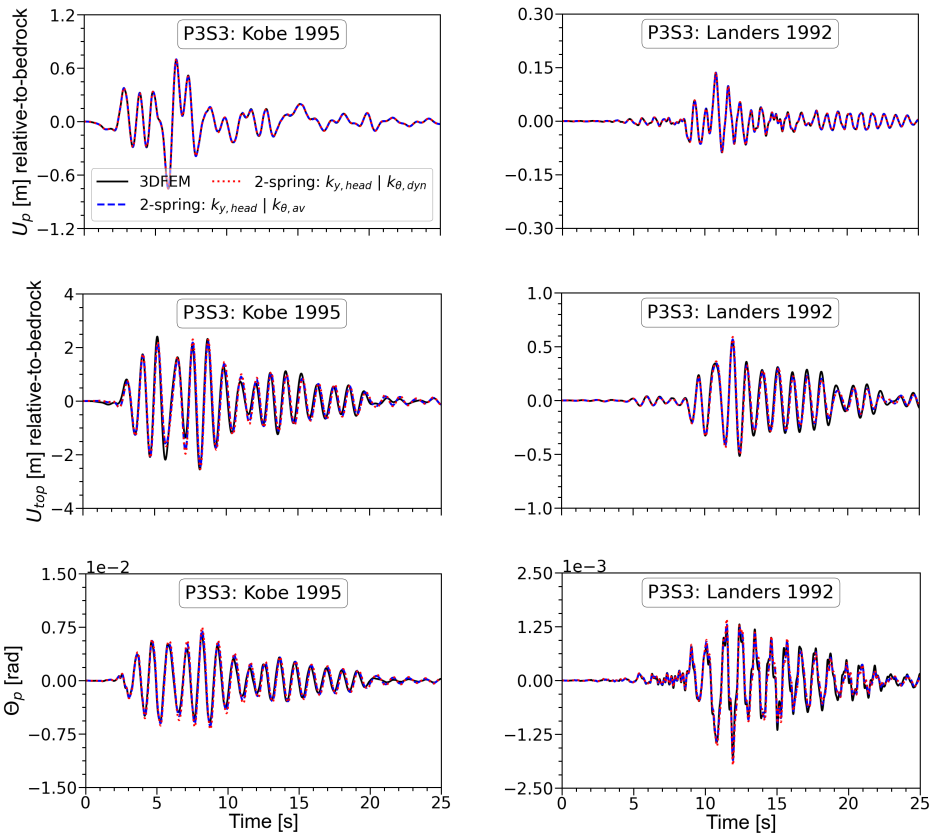

Figure 3.15: P3S3 pile head and superstructure time histories for earthquakes Kobe and Landers

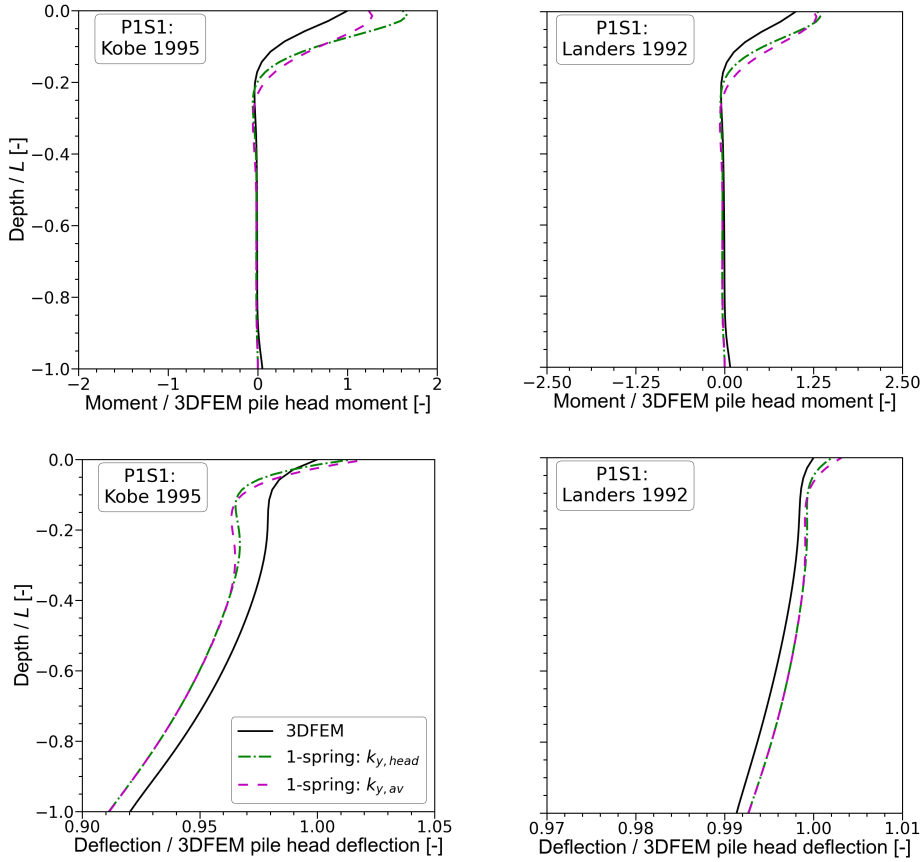

Figure 3.16: P1S1 moment and deflection profiles at maximum pile head displacement for earthquakes Kobe and Landers

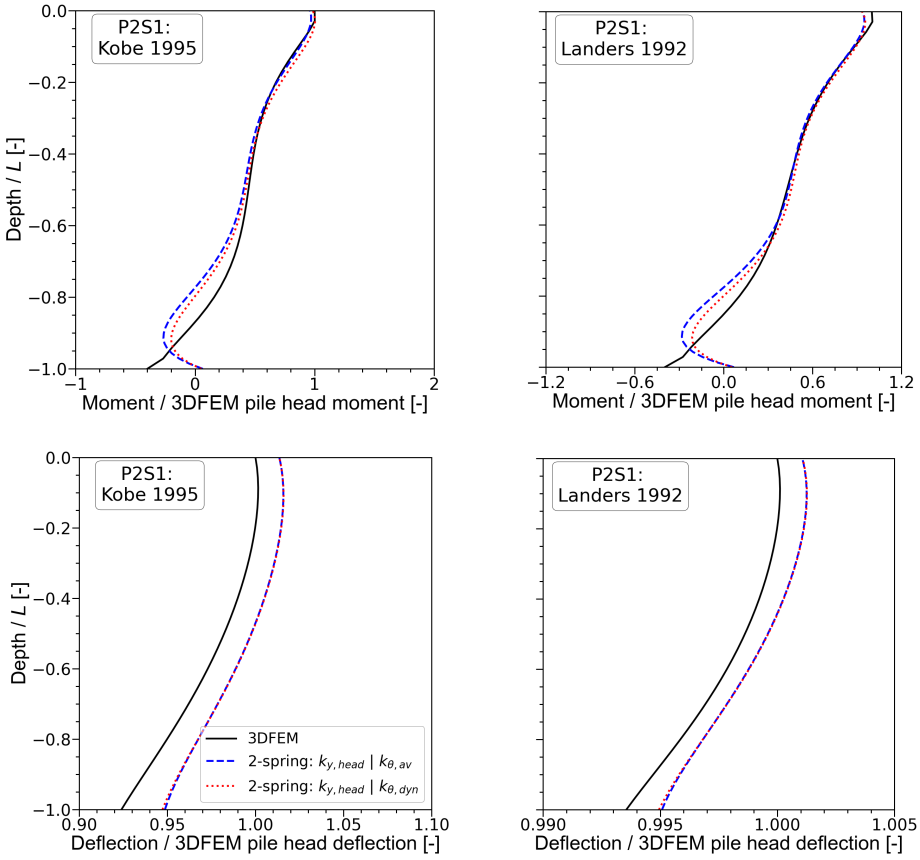

Figure 3.17: P2S1 moment and deflection profiles at maximum pile head displacement for earthquakes Kobe and Landers

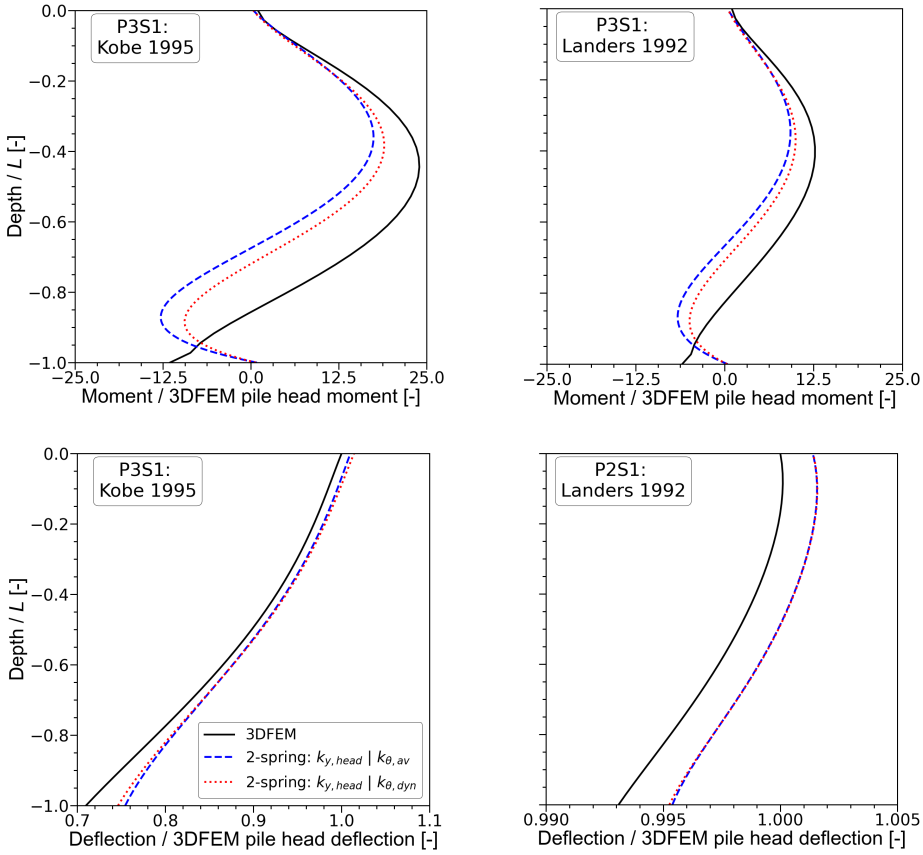

Figure 3.18: P3S1 moment and deflection profiles at maximum pile head displacement for earthquakes Kobe and Landers

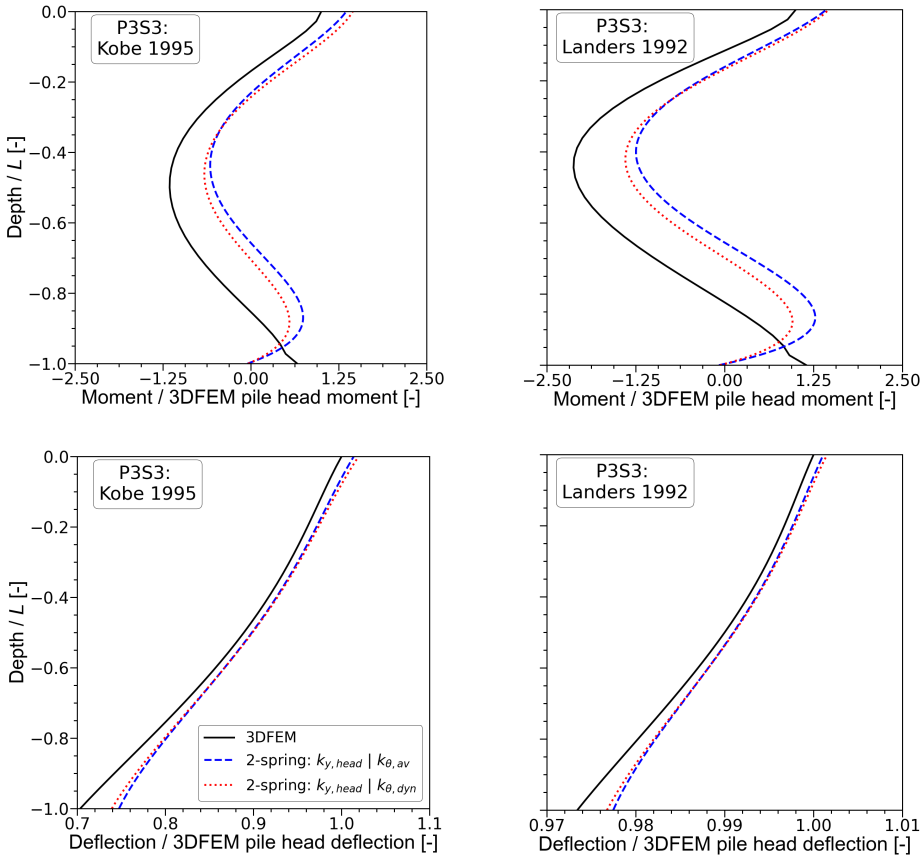

Figure 3.19: P3S3 moment and deflection profiles at maximum pile head displacement for earthquakes Kobe and Landers

Chapter 4

Conclusions & Recommendations

4.1 Conclusions

In this report the dynamic interaction of soil-monopile-superstructure systems is first examined (Chapter 2). Conclusions are reached regarding the inertial and kinematic interaction effects:

- Inertial interaction:
  - Dictates the dynamic response around the 1st natural frequency of the system, $f_{0,\mathrm{SSI}}$ (Figure 2.7);
  - Given the pile head loading due to the superstructure inertial loading, the monopiles are stressed near their head in terms of deflection (Figure 2.8, [14]). In case of the non-slender piles like monopiles P2 and P3 examined in this report (Table 1.2), the rotation not only near the pile head but also to greater depths is expected to be affected (Figure 2.8);
  - Its effect on the dynamic response depends on the superstructure mass and stiffness in comparison to the monopile rigidity (i.e. superstructure S3 has higher effect on monopile P3, than superstructure S1, as shown in Figure 2.7).

- Kinematic interaction:
  - Dictates the dynamic response after $f_{0,\text{SSI}}$ (Figure 2.7);
  - Given the nature of this type of loading -distributed over the pile length- all monopiles are stressed over depth (Figure 2.8);
  - The amplitude of both the pile head deflection and rotation depends on the ratio between the pile length and the wavelength of the mono-harmonic excitation, together with the relative pile-soil rigidity (i.e. K_{r}).

In Chapter 3, the calibration of the 1D FE models based on monotonic pile head loading and their prediction of the dynamic interaction and seismic response are examined. Based on the observations made in this chapter, it can be concluded:

- Static p-y and m-θ spring stiffness values uniform along the monopile length, based on pile head loading:
  - The p-y spring stiffness increases with the monopile diameter (Table 3.1, Figure 3.3). As the diameter increase is associated to the L/D decrease for the monopiles examined herein, further research is needed to account for the diameter and L/D effect separately;
  - The m-θ spring stiffness is proportional to D^2, verifying the dependence of the distributed moment on the shear vertical stresses which develop at the monopile periphery. Regarding the L/D effect, k_θ is independent of L/D for the two non-slender monopiles examined herein, with L/D=9 and 5. While the stiffness of the distributed moment-rotation springs is L/D-dependent for caisson foundations [17, 33], monopiles of lower L/D ratios should be examined to assess the effect of L/D on k_θ for stubbier monopiles;
  - Both k_{y} and k_θ depend on the response to be matched; pile head or average-over-depth response. Matching the latter results in lower values (Table A.1).
- Soil reaction components to be accounted for in the 1D FE modelling of the dynamic soil-monopile-superstructure interaction:
  - In case of the slender monopile P1 with L/D=26, the pile head and superstructure response is in general well captured throughout the examined frequency range when employing p-y springs alone (Figures 3.4). A

good match is in general achieved also in case of the monopile moment and deflection distribution over depth (Figures 3.7 and A.2). However, the biggest deficiency of the models applied herein is the prediction of the pile head rotation amplitude for frequencies higher than $f_{0,\text{SSI}}$, together with the pile head and base moment;

- In case of the non-slender monopiles P2 and P3 with L/D=9 and 5, respectively, the distributed moment resistant mechanism (i.e. m-θ springs) should be accounted for in 1D FE models to capture the pile head and superstructure response (Figures 3.4 and 3.6). The employment of m-θ springs mainly affects the response at frequencies where the kinematic interaction is dominant (Figure A.1). Regarding the deflection and moment profiles, in case of P2, the p-y and m-θ springs provide a good prediction, except for the base moment. In case of monopile P3, the base shear and moment seem important for the response over depth;
- The distributed moment resistant mechanism affects the dynamic response mainly for frequencies higher than $f_{0,\text{SSI}}$, for which the kinematic interaction dominates the response. In other words, changing k_θ does not practically affect the prediction of the 1D FE model around $f_{0,\text{SSI}}$ (Figure A.1);
- The calibration of the soil reaction components based on the monotonic pile head loading and their use throughout the examined frequency range provide a satisfying match between the 3D and 1D prediction of the system dynamic interaction (i.e. steady state response under mono-harmonic excitation).

- 3D-to-1D modelling of seismic response:
  - In case of monopile P1, there is a mismatch between 3D and 1D regarding the monopile rotation and superstructure displacement. This is attributed to the underprediction of the system's fundamental frequency (Section 3.2.2.2), in addition to the slight mismatch already observed in case of the steady-state dynamic response (Figure 3.4). This means that the hereby calibration procedure (i.e. monotonic pile head loading, uniform stiffness along the monopile length) is not suitable for the 1D FE modelling of the seismic response of this slender monopile;
  - In case of the non-slender monopiles P2 and P3, the superstructure displacement and pile head deflection and rotation with time are sufficiently predicted when employing the *2-spring* models calibrated based on monotonic lateral pile head loading. Regarding the moment and deflection

profiles, the match is good near the pile head. However, according to the previous conclusions, the base effect should be considered, especially for monopile P3;

- The divergence of the 1D FE results from the 3D ones seems independent of the frequency content of the seismic excitation (Figure 1.8);
- Considering a different superstructure on top of monopile P3 (i.e. S1 and S3) affects the match between 3D and 1D regarding the moment distribution near the pile head (Figures 3.18 and 3.19), something which is not true for the dynamic interaction (Section 3.2.2.1). In particular, although for P3S1 the bending moment values near the pile head are well-predicted by the 1D models, this is not true for P3S3;
- The radiation damping and inertia of the soil mass are not modelled in the 1D FE models employed herein and this seems to have no effect on the dynamic response of the systems.

4.2 Recommendations

Based on the results regarding the match between the 3D and 1D FE modelling of the dynamic interaction and seismic response of the hereby examined soil-monopile-superstructure systems, the following topics are suggested for further research:

- Static p-y and m-θ spring stiffness values uniform over depth, based on pile head loading:
  - Examination of a greater number of monopiles of different diameters and rigidities to conclude on the diameter and L/D effect on the p-y spring stiffness;
  - Examination of monopiles of lower L/D ratios to assess the L/D effect on the k_θ values.
- Calibration of the soil reaction curves for the 1D FE modelling of the dynamic response:
  - In case of a uniform linear elastic soil layer, spring stiffness values varying with depth should be considered to examine whether the moment and deflection profiles are better predicted for all the monopiles examined herein (i.e. P1, P2 and P3). It should also be examined whether

the consideration of different calbration procedures results in better prediction of the fundamental frequency of the soil-monopile-superstructure systems in case of P1 and thus ameliorates the prediction of the superstructure and monopile head response with time;

- In case of a non-uniform, non-linear elasto-plastic soil layer, the calibration of the soil reaction curves based on monotonic pile head loading should be examined. This is already performed by Rahmani et al. [29] in case of slender piles with the use of p-y springs. In case of non-slender monopiles, *2-spring* models should be considered and the calibration procedure suggested herein ($k_{\text{y,head}}$ & $k_{\theta,\text{av}}$) could be applied. Furthermore, in case of two-phased sand layers, with pore water present, which is the case for OWTs, the negative effect of the excess pore pressures on the spring stiffness should be considered;
- Calibration procedures for the base translational and rotational components should be developed. Next, the monopile rigidities for which each of these two components becomes important should be assessed. This has already been done in case of analytical solutions for poro-visco-elastic soil [20]. The hereby report sheds some light on that, but more monopiles need to be examined, after accurately calibrating the base translational and rotational springs.

- Radiation damping and inertial loading of the soil mass in the vicinity of the monopile:
  - Ignoring the radiation damping and inertia of the soil mass seems to have no effect in case of the linear elastic soil examined herein. Their effect when non-linear elasto-plastic soils are modelled should be examined [29].

- Other suggestions:
  - In this report, the categorization of the monopiles is done based on their geometrical properties (i.e. monopile embedded length and diameter) and the soil layer stiffness, which are considered in the definition of the pile relative stiffness (K_{r}, Section 1.2.2). The deflection and rotation over depth of a particular monopile depends on the excitation wavelength relative to its length (Figure 2.5) proving the p-y springs enough for the prediction of the response of non-slender piles at high-frequency excitations (Figures 3.4 and 3.5). Therefore, in case of a seismic excitation, a 'dynamic slenderness' based on the monopile length and wavelength of

the dominant frequency of the excitation should be defined to predict the behaviour of the monopile and the spring components that need to be considered;

– The consideration of superstructures which are representative of OWTs should be considered to examine whether the 1D prediction of the seismic response is accurate, given the observed superstructure effect on the pile head moment (Figures 3.18 and 3.19).

References

[1] Abadie, C. N. (2015). *Cyclic Lateral Loading of Monopile Foundations in Cohesionless Soils*. [Doctoral dissertation, University of Oxford]

[2] Anoyatis, G., Di Laora, R., Mandolini, A., & Mylonakis, G. (2013). Kinematic response of single piles for different boundary conditions: Analytical solutions and normalization schemes. *Soil Dynamics and Earthquake Engineering*, *44*, 183–195

[3] API. (2002). *Recommended Practice for Planning, Designing and Constructing Fixed Offshore Platforms—Working Stress Design*

[4] Ashford, S. A. & Juirnarongrit, T. (2003). Evaluation of pile diameter effect on initial modulus of subgrade reaction. *Journal of Geotechnical and Geoenvironmental Engineering*, *129*(3), 234–242

[5] Baguelin, F., Frank, R., & Saïd, Y. H. (1977). Theoretical study of lateral reaction mechanism of piles. *Géotechnique*, *27*(3), 405–434

[6] Bhattacharya, S., Biswal, S., Aleem, M., Amani, S., Prabhakaran, A., Prakhya, G., Lombardi, D., & Mistry, H. K. (2021). Seismic design of offshore wind turbines: Good, bad and unknowns. *Energies*, *14*. https://doi.org/10.3390/en14123496

[7] Bhattacharyaa, S., De Risi, R., Lombardi, D., Ali, A., Demirci, H. E., & Haldar, S. (2021). On the seismic analysis and design of offshore wind turbines. *Soil Dynamics and Earthquake Engineering*, *145*. https://doi.org/10.1016/j.soildyn.2021.106692

[8] Boulanger, R. W., Curras, C. J., Kutter, B. L., Wilson, D. W., & Abghari, A. (1999). Seismic soil-pile-structure interaction experiments and analyses. *Journal of Geotechnical and Geoenvironmental Engineering*, *125*(9), 750–759

[9] Burd, H. J., Taborda, D. M. G., Zdravković, L., Abadie, C. N., Byrne, B. W., Houlsby, G. T., Gavin, K. G., Igoe, D. J. P., Jardine, R. J., & More Authors (2020). Pisa design model for monopiles for offshore wind turbines: application to a marine sand. *Géotechnique*, 70(11), 1048–1066. https://doi.org/10.1680/jgeot.18.P.277

[10] Byrne, B. W., McAdam, R., Burd, H. J., Houlsby, G. T., Martin, C. M., Zdravković, L., Taborda, D. M. G., Potts, D. M., Jardine, R. J., Sideri, M., Schroeder, F. C., Gavin, K., Doherty, P., Igoe, D., Muir Wood, A., Kallehave, D., & Skov Gretlund, J. (2015). New design methods for large diameter piles under lateral loading for offshore wind applications. *Proceedings of the Third International Symposium on Frontiers in Offshore Geotechnics (ISFOG 2015), Oslo, Norway*.

[11] Chopra, A. K. (1995). *Dynamic of Structures: Theory and Applications to Earthquake Engineering*. Prentice Hall

[12] DNV. (2020, February 11). *Offshore wind power expands globally*. https://www.dnv.com/expert-story/maritime-impact/Offshore-wind-power-expands-globally.html

[13] Fan, K. & Gazetas, G. (1991). Seismic response of single piles and pile groups. *NATIONAL CENTER FOR EARTHQUAKE ENGINEERING RESEARCH*, Technical Report NCEER-91-0003

[14] Gazetas, G. (1984). Seismic response of end-bearing single piles. *Soil Dynamics and Earthquake Engineering*, *3*(2)

[15] Gazetas, G. & Dobry, R. (1984a). Horizontal response of piles in layered soils. *Journal of Geotechnical Engineering*, *110*(1), 20–40

[16] Gazetas, G. & Dobry, R. (1984b). Simple radiation damping model for piles and footings. *Journal of Geotechnical Engineering*, *110*(6), 937–956

[17] Gerolymos, N. & Gazetas, G. (2006). Winkler model for lateral response of rigid caisson foundations in linear soil. *Soil Dynamics and Earthquake Engineering*, *26*, 347–361

[18] Griffiths, D. V. (1989). Advantages of consistent over lumped methods for analysis of beams on elastic foundations. *Communications in applied numerical methods*, *5*, 53–60

[19] He, R., Kaynia, A. M., & Zhanga, J. (2019). A poroelastic solution for dynamics of laterally loaded offshore monopiles. *Ocean Engineering*, *179*, 337–350. https://doi.org/10.1016/j.oceaneng.2019.02.068

[20] He, R., Kaynia, A. M., & Zhu, T. (2021). Effect of base shear and moment on lateral dynamic behavior of monopiles. *Ocean Engineering*, *228*. https://doi.org/10.1016/j.oceaneng.2021.108957

[21] Kagawa, T. (1992). Modeling soil reaction to laterally loaded piles. *Transportation Research Record*

[22] Kaynia, A. M. (2019). Seismic considerations in design of offshore wind turbines. *Soil Dynamics and Earthquake Engineering*, *124*. https://doi.org/10.1016/j.soildyn.2018.04.038

[23] Kaynia, A. M. (2020). Effect of kinematic interaction on seismic response of offshore wind turbines on monopiles. *Earthquake Engineering and Structural Dynamics*, *50*, 777–790. https://doi.org/10.1002/eqe.3371

[24] Kramer, S. L. (1996). *Geotechnical Earthquake Engineering*. Prentice Hall

[25] Lehane, B. M. & White, D. J. (2005). Lateral stress changes and shaft friction for model displacement piles in sand. *Canadian Geotechnical Journal*, *42*, 1039–1052

[26] Ling, L. F. (1988). Back analysis of lateral load test on piles. *University of Auckland Report No. 460*

[27] Medina, C., Álamo, G. M., & Quevedo-Reina, R. (2021). Evolution of the seismic response of monopile-supported offshore wind turbines of increasing size from 5 to 15 mw including dynamic soil-structure interaction. *Journal of Marine Science and Engineering*, *9*. https://doi.org/10.3390/jmse9111285

[28] Patra, S. K. & Haldar, S. (2021). Seismic response of monopile supported offshore wind turbine in liquefiable soil. *Structures*, *31*. https://doi.org/10.1016/j.istruc.2021.01.095

[29] Rahmani, A., Taiebat, M., Liam Finn, W. D., & Ventura, C. E. (2018). Evaluation of p-y springs for nonlinear static and seismic soil-pile interaction analysis under lateral loading. *Soil Dynamics and Earthquake Engineering*, *115*, 438–447. https://doi.org/10.1016/j.soildyn.2018.07.049

[30] Randolph, M. & Gourvenec, S. (2011). *Offshore Geotechnical Engineering*. Taylor & Francis

[31] Sørensen, S. P. H., Brødbæk, K. T., & Møller, M. (2009). Evaluation of load-displacement relationships for large-diameter piles. *Faculties of Engineering, Science and Medicine, Aalborg University*

[32] Turner, B. J., Brandenberg, S. J., & Stewart, J. P. (2017). Influence of kinematic ssi on foundation input motions for bridges on deep foundations. *Pacific Earthquake Engineering Research Center*, PEER Report No. 2017/08

[33] Varun, Assimaki, D., & Gazetas, G. (2009). A simplified model for lateral response of large diameter caisson foundations—linear elastic formulation. *Soil Dynamics and Earthquake Engineering*, *29*, 268–291

[34] Versteijlen, W. G., Metrikine, A. V., & van Dalen, K. N. (2016). A method for identification of an effective winkler foundation for large-diameter offshore wind turbine support structures based on in-situ measured small-strain soil response and 3d modelling. *Engineering Structures*, *124*, 221–236. http://dx.doi.org/10.1016/j.engstruct.2016.06.007

[35] Watanabe, K., Pisanò, F., & Jeremić, B. (2017). Discretization effects in the finite element simulation of seismic waves in elastic and elastic-plastic media. *Engineering with Computers*, *33*, 519–545. https://link.springer.com/article/10.1007/s00366-016-0488-4

[36] Wind Europe (2020, February). *Offshore Wind in Europe: Key trends and statistics 2019*. https://windeurope.org/wp-content/uploads/files/about-wind/statistics/WindEurope-Annual-Offshore-Statistics-2019.pdf

Appendix A

Further Results

A.1 Effect of different monotonic calibration of *2-spring* models on the dynamic response

In addition to the $k_{\text{y,head}}$-$k_{\text{theta,av}}$ spring stiffnesses used in the 1D *2-spring* models, two other combinations of spring stiffnesses are considered: $k_{\text{y,head}}$-$k_{\theta,\text{head}}$, and $k_{\text{y,av}}$-$k_{\text{theta,av}}$. These m-θ spring stiffnesses are calculated based on the pile head or average-over-depth rotation when considering $k_{\text{y,head}}$ or $k_{\text{y,av}}$, respectively. This procedure is similar to the one described in Section 3.1.1.

The values of the above-mentioned spring stiffnesses are presented in Table A.1, while Figure A.1 shows the dynamic response of P2S1 when these stiffnesses are considered. It is observed that both new k_θ values are higher than $k_{\theta,\text{av}}$ calculated for $k_{\text{y,head}}$. According to Figure A.1, it is the rotational spring stiffness that affects the response of monopile P2 for frequencies higher than $f_{0,\text{SSI}}$, as expected (Figure 2.8).

Table A.1: Spring stiffness values for different k_y - k_θ combinations

Pile	$k_{\text{y,head}}/G_{\text{soil}}$ [-]	$k_{\text{y,av}}/G_{\text{soil}}$ [-]	$k_{\theta,\text{head}}/(G_{\text{soil}}D^2)$ [-] (for $k_{\text{y,head}}$)	$k_{\theta,\text{av}}/(G_{\text{soil}}D^2)$ [-] (for $k_{\text{y,av}}$)
P1	6.5	2.8	-	-
P2	7.0	3.0	2.3	2.5 (1.3 for $k_{\text{y,head}}$)
P3	7.5	3.8	2.3	2.5 (1.3 for $k_{\text{y,head}}$)

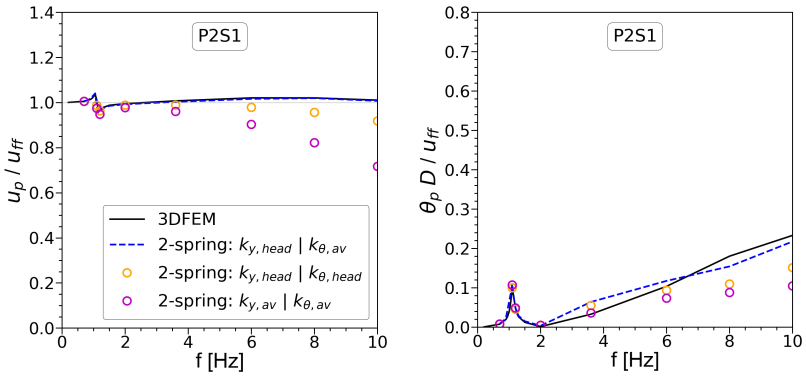

Figure A.1: P2S1 dynamic interaction for the k_y - k_θ combinations of Table A.1

A.2 Moment and deflection profiles for f=6.0Hz

A.2.1 *1-spring* and *2-spring* models

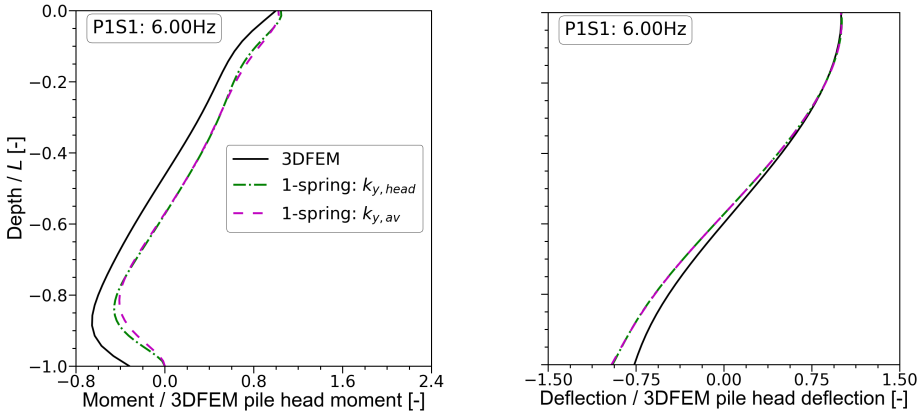

Figure A.2: P1S1 moment and deflection profiles for excitation frequency f = 6.0Hz

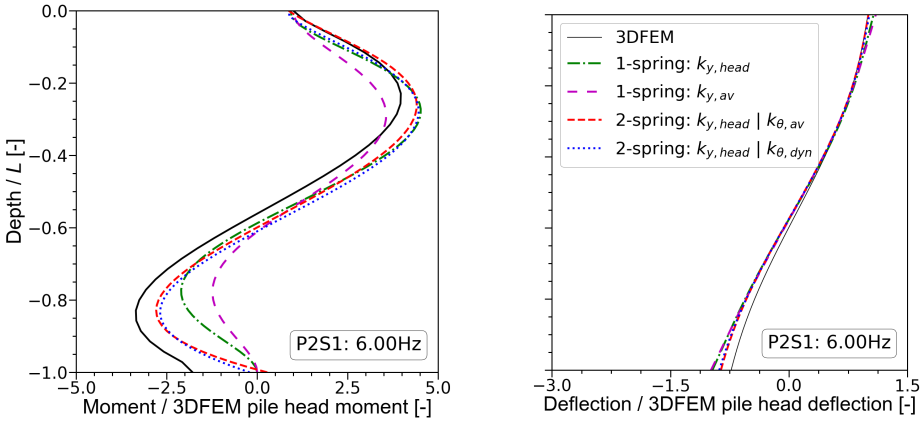

Figure A.3: P2S1 moment and deflection profiles for excitation frequency f = 6.0Hz

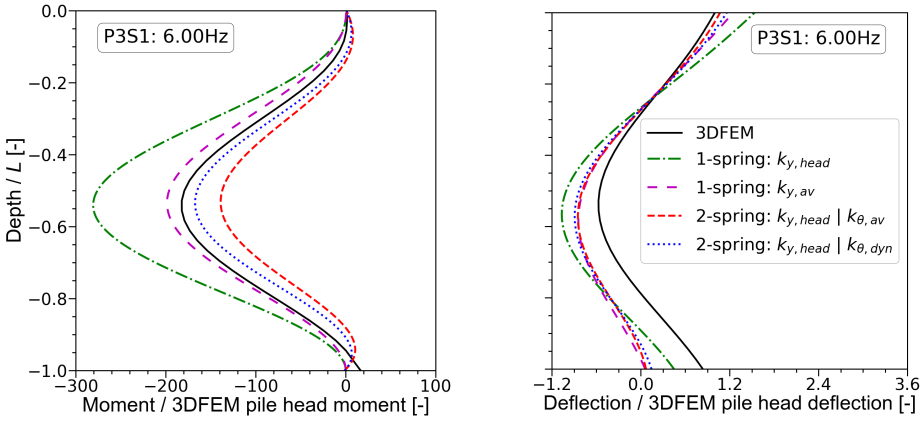

Figure A.4: P3S1 moment and deflection profiles for excitation frequency f = 6.0Hz

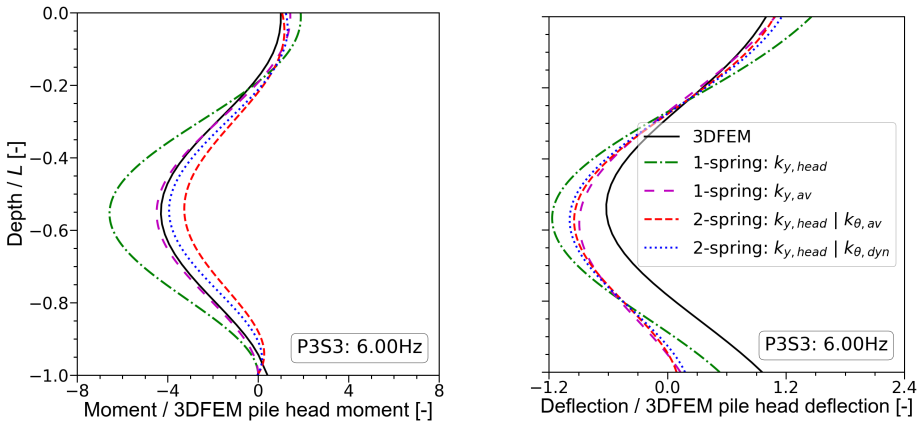

Figure A.5: P3S3 moment and deflection profiles for excitation frequency f = 6.0Hz

A.2.2 Base effect

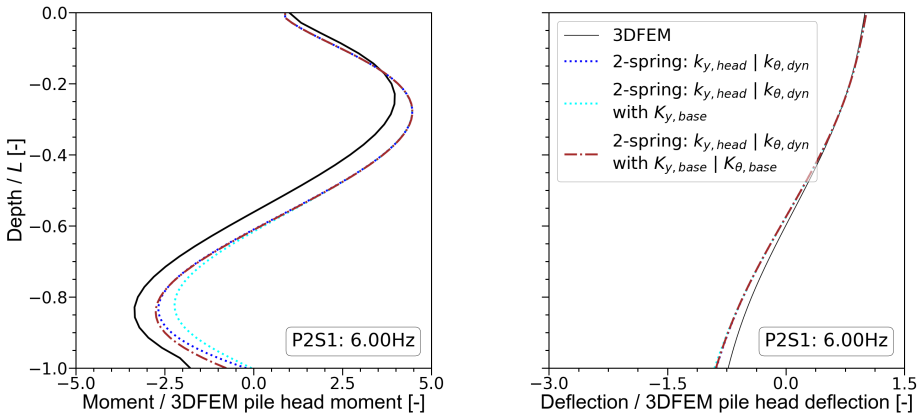

Figure A.6: P2S1 base effect for excitation frequency f = 6.0Hz

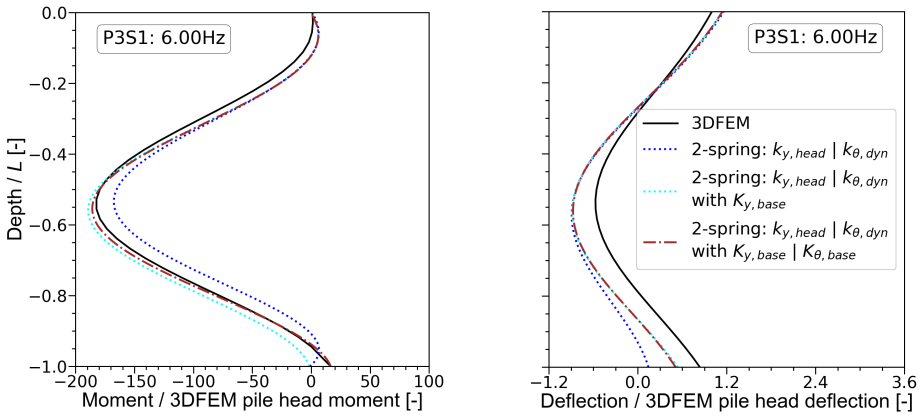

Figure A.7: P3S1 base effect for excitation frequency f = 6.0Hz